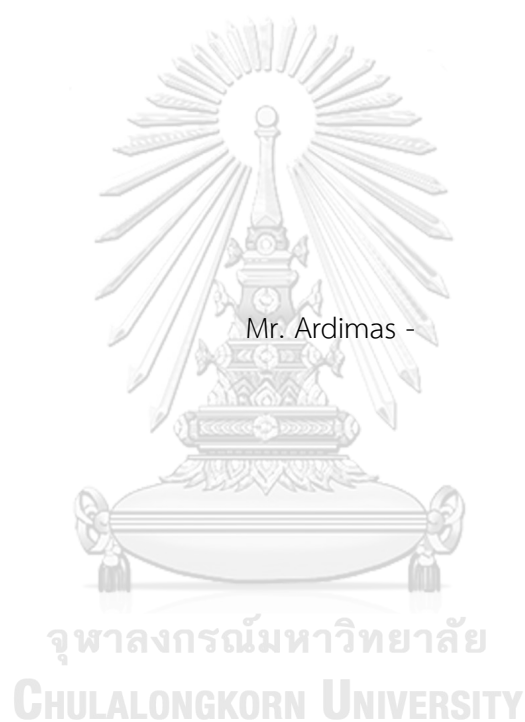


High-Pressure Study of Hybrid Organic-Inorganic Perovskites and Double Perovskites



A Dissertation Submitted in Partial Fulfillment of the Requirements
for the Degree of Doctor of Philosophy in Nanoscience and Technology

Inter-Department of Nanoscience and Technology

GRADUATE SCHOOL

Chulalongkorn University

Academic Year 2022

Copyright of Chulalongkorn University



จุฬาลงกรณ์มหาวิทยาลัย
CHULALONGKORN UNIVERSITY

การศึกษาไฮบริดเพอร์ออฟสโงัดอินทรีย์และอนินทรีย์แบบคู่ภายใต้ความดันสูง



วิทยานิพนธ์นี้เป็นส่วนหนึ่งของการศึกษาตามหลักสูตรปริญญาวิทยาศาสตรดุษฎีบัณฑิต
สาขาวิชาวิทยาศาสตร์นาโนและเทคโนโลยี สหสาขาวิชาวิทยาศาสตร์นาโนและเทคโนโลยี

บัณฑิตวิทยาลัย จุฬาลงกรณ์มหาวิทยาลัย

ปีการศึกษา 2565

ลิขสิทธิ์ของจุฬาลงกรณ์มหาวิทยาลัย

Thesis Title High-Pressure Study of Hybrid Organic-Inorganic
Perovskites and Double Perovskites
By Mr. Ardimas -
Field of Study Nanoscience and Technology
Thesis Advisor Associate Professor Thiti Bovornratanaraks, Ph.D.
Thesis Co Advisor Assistant Professor SOJIPHONG CHATRAPHORN, Ph.D.

Accepted by the GRADUATE SCHOOL, Chulalongkorn University in Partial
Fulfillment of the Requirement for the Doctor of Philosophy

..... Dean of the GRADUATE SCHOOL
(Associate Professor YOOTTHANA CHUPPUNNARAT, Ph.D.)

DISSERTATION COMMITTEE

..... Chairman
(Associate Professor Rachsak Sakdanuphab, Ph.D.)

..... Thesis Advisor
(Associate Professor Thiti Bovornratanaraks, Ph.D.)

..... Thesis Co-Advisor
(Assistant Professor SOJIPHONG CHATRAPHORN, Ph.D.)

..... Examiner
(Associate Professor NAKORN PHAISANGITTISAKUL, Ph.D.)

..... Examiner
(Assistant Professor ANNOP EKTARAWONG, Ph.D.)

..... Examiner
(Assistant Professor RATTHAPOL RANGKUPAN, Ph.D.)

..... Examiner
(Associate Professor NUTTHITA CHUANKRERKKUL, Ph.D.)

..... Examiner
(Assistant Professor SUKKANESTE TUNGASMITA, Ph.D.)

อาร์ติมีส - :

การศึกษาไฮบริดเพอโรฟสไกต์อินทรีย์และอนินทรีย์แบบคู่ภายใต้ความดันสูง. (High-Pressure Study of Hybrid Organic-Inorganic Perovskites and Double Perovskites) อ.ที่ปรึกษาหลัก : รศ. ดร.ฉติ บวรรัตน์รักษ์, อ.ที่ปรึกษาร่วม : ผศ. ดร.โคจิพงศ์ ฉัตรภรณ์

ไม่นานมานี้วัสดุเพอโรฟสไกต์ชนิดลูกผสมและดับเบิล (Hybrid and double perovskites) ได้กลายมาเป็นจุดสนใจของงานวิจัยทางด้านออปโต อิเล็กทรอนิกส์เนื่องด้วยสมบัติเชิงฟิสิกส์และเคมีที่มีศักยภาพ อย่างไรก็ตามการพัฒนาความสามารถเชิงแสงของวัสดุชนิดนี้ยังคงเป็นความท้าทายในงานวิจัยนี้ผู้วิจัยได้ศึกษาการเปลี่ยนแปลงที่ขึ้นกับความดันซึ่งเป็นหนึ่งในวิธีในการพัฒนาสมบัติเชิงออปโตอิเล็กทรอนิกส์ผู้วิจัยได้ประสบความสำเร็จในการสังเคราะห์สารเพอโรฟสไกต์ชนิดลูกผสม $\text{CH}_3\text{NH}_3\text{PbI}_3$ และดับเบิลเพอโรฟสไกต์ Cs_2TiBr_6 โดยใช้เทคนิคการเตรียมที่มีชื่อว่า inverse temperature crystallization และวิธีการทางเคมี ผู้วิจัยได้ศึกษาการเปลี่ยนแปลงและสมบัติการเปล่งแสงที่ขึ้นกับความดันของวัสดุทั้งสองชนิด โดยนำตัวอย่างวางไปที่ diamond anvil cells เพื่อทำการอัดแรงดันและใช้เทคนิคทางรามานในการวัดสมบัติการเปล่งแสงเพื่อเป็นการสนับสนุนผลที่ได้จากการทดลองผู้วิจัยยังได้ทำการคำนวณแบบ first-principles ผลการศึกษาพบว่า MAPbI_3 เปลี่ยนเฟสถึง 3 ครั้งภายใต้ความดันที่สูงถึง 5.34 GPa การเปลี่ยนแปลงจากเฟสเชิงผลวัดไปสู่เฟสเชิงสถิตเกิดขึ้นที่ความดัน 3.26 GPa การหายไปของสารสันของโมเลกุลอินทรีย์ CH_3NH_3 เกิดขึ้นในเฟสเชิงสถิต ทั้งนี้ผู้วิจัยยังได้พบถึงการเปลี่ยนรูปร่างของ Cs_2TiBr_6 ด้วยกระบวนการทดลองที่เหมือนกัน อย่างไรก็ตาม Cs_2TiBr_6 เปลี่ยนเฟสที่ความดัน 11.9 GPa นอกจากนี้จุดยอดระนาบใหม่ของ TiBr_6 ที่มีโครงสร้างเป็นทรงแปดหน้าถูกตรวจเจอและบ่งบอกถึงอันตรกิริยาที่มีความเข้มสูงและการเปลี่ยนแปลงจากเฟสอัลฟาสู่เฟสบีต้า หลังจากการนั้นการเปล่งแสงเชิงรามานของวัสดุยังเกิดการเลื่อนไปทางแดงเช่นเดียวกันกับการเกิดจุดยอดระนาบที่กว้างขึ้นอย่างมีนัยสำคัญภายใต้ความดันที่สูงขึ้นจนถึง 12.6 GPa.

สาขาวิชา วิทยาศาสตร์นาโนและเทคโนโลยี ลายมือชื่อนิสิต

ยี่

ปีการศึกษา 2565

ลายมือชื่อ อ.ที่ปรึกษาหลัก

ลายมือชื่อ อ.ที่ปรึกษาร่วม

6288808520 : MAJOR NANOSCIENCE AND TECHNOLOGY

KEYWORD: High pressure, Hybrid perovskite, Double perovskite, Phase transition, Raman spectroscopy, DFT, First principles

Ardimas - : High-Pressure Study of Hybrid Organic-Inorganic Perovskites and Double Perovskites. Advisor: Assoc. Prof. Thiti Bovornratanaraks, Ph.D. Co-advisor: Asst. Prof. SOJIPHONG CHATRAPHORN, Ph.D.

Hybrid and double perovskite have been of great attraction for optoelectronic devices. However, exploring a feasible method to enhance their optical abilities remains a considerable challenge. Here, the researcher reports the pressure-induced phase transition as an effective way to modify optoelectronic properties. The researcher successfully synthesized the hybrid perovskite (MAPbI₃) and the double perovskite (Cs₂TiBr₆) by the inverse temperature crystallization (ITC) and solution method, respectively. The researcher studied the pressure dependence phase transition and photoluminescence (PL) by placing the sample into diamond anvil cells (DACs) through Raman spectroscopy. The first principles method was used to support the idea. The researcher observed at least 3 phase transition of MAPbI₃ under hydrostatic compression up to 5.34 GPa. The transformation from dynamic to static phases occurs at 3.26 GPa. The static phase shows the disappearance of organic CH₃NH₃ vibration. The researcher also observed the structural deformation of Cs₂TiBr₆ by a similar method. However, Cs₂TiBr₆ exhibit a distinct phase transition under high pressure of 11.9 GPa. New Raman peaks of octahedral TiBr₆ indicate high interaction and indicate the evolution from alpha phase to beta phase. Subsequently, the emission undergoes a red shift and a significant broadening under further pressure up to 12.6 GPa.

Field of Study: Nanoscience and
Technology

Student's Signature

Academic Year: 2022

Advisor's Signature

Co-advisor's Signature

ACKNOWLEDGEMENTS

“In the name of Allah, the Most Gracious and the Most Merciful”

Alhamdulillah, all praises and thanks belong to Allah may He be glorified and exalted. May Allah's peace and blessing be upon our Beloved Prophet Muhammad who was a mercy for granting me the chance and the ability to successfully complete this study.

I am really grateful to everyone for their encouragement and assistance throughout my Doctoral studies and related research. This thesis would not have been accomplished without their assistance.

First and foremost, I want to thank my adviser, Associate Professor Dr. Thiti Bovornratanaraks, for his advice, patience, and support. I also like to thank Assistant Professor Dr. Sojiphong Chatraphorn for always encouraging me in my efforts. I feel really blessed to be able to work with such a thoughtful and supportive professor. I won't be able to complete my studies at Chulalongkorn University without them offering to carry out this research.

I would like to express my sincere thanks to my research committee members, Assoc. Prof. Dr. Rachsak Sakdanuphab from the Department of Physics at King Mongkut Institute of Technology Ladkrabang, and Asst. Prof. Dr. Sukkaneste Tungasmita, Assoc. Prof. Dr. Nakorn Phaisangittisakul, Asst. Prof. Dr. Annop Ektarawong from the Department of Physics and also Asst. Prof. Dr. Ratthapol Rangkupan and Assoc. Prof. Dr. Nutthita Chuankrerkkul from Nanoscience and Technology Program for providing me with comments that greatly improved my research work.

I would also want to thank everyone for working at the Extreme Condition Physics Research Laboratory (ECPRL) and the Semiconductor Physics Research Laboratory (SPRL) for their cooperation, motivation, and friendship.

I would like to express my gratitude to the Chulalongkorn 2nd Century Found (C2F) scholarship awards at Chulalongkorn University in Thailand for making this effort possible.

Last but not least, I would want to express my gratitude and respect to my

parents, Siswi Yulianti and Djoko Soemartono, for their unwavering support. Thank you for giving me the courage to reach for the stars and pursue my dream. My warmest gratitude also goes to my big brother, Armanda. I would want to express my gratitude to my wife, Yunita Dewi Nugraheni, for her love and support over the years.

Ardimas -



TABLE OF CONTENTS

	Page
ABSTRACT (THAI).....	iii
ABSTRACT (ENGLISH).....	iv
ACKNOWLEDGEMENTS	v
TABLE OF CONTENTS	vii
LIST OF TABLES	ix
LIST OF FIGURES	x
CHAPTER 1.....	1
INTRODUCTION	1
1.1. Background	1
1.2. Aims of The Research.....	6
1.3. Research Flow.....	7
1.4. Thesis Structure.....	8
CHAPTER 2.....	10
LITERATURE REVIEW	10
2.1. Photovoltaic (PV).....	10
2.2. Perovskites	13
2.3. Hybrid Organic-Inorganic Perovskites.....	15
2.4. Double Perovskites.....	19
2.5. High-Pressure Technology.....	21
2.6. Structural and Phase Evolution.....	25
2.7. Electronic and Physical Evolution.....	28

2.8. Density Functional Theory.....	32
CHAPTER 3.....	39
RESEARCH FRAMEWORK	39
3.1. Materials Preparation.....	39
3.1.1. MAPbI ₃ Single Crystal.....	39
3.1.2. Cs ₂ TiBr ₆ Single Crystal.....	40
3.2. Experimental Method.....	41
3.2.1. High Pressure Technique.....	41
3.2.2. The Fundamentals of Raman Spectroscopy.....	42
3.3. Computational Method.....	44
CHAPTER 4.....	46
RESULT AND DISCUSSION.....	46
4.1. Hybrid Organic-Inorganic Perovskites.....	46
4.2. Lead-Free Double Perovskites.....	54
4.3. Phase Transition under Pressure.....	59
4.4. Optical Properties under Pressure.....	76
CHAPTER 5.....	82
CONCLUSION	82
REFERENCES.....	84
VITA.....	94

LIST OF TABLES

	Page
Table 1. Symmetry, calculated Raman, and observed Raman as well as vibrational characters.....	51



LIST OF FIGURES

	Page
Figure 1. World solar photovoltaic cost through the years (EIA, 2021).	11
Figure 2. Classification of photovoltaic technology.....	12
Figure 3. Perovskite structure based ion oxides (Yoshimura & Sardar, 2021).....	13
Figure 4. Conversion efficiency of solar cells with various materials (EIA, 2021).	14
Figure 5. Hybrid organic inorganic perovskite structure (a) (Cho et al., 2021) and the structural differences between Inorganic with hybrid perovskite (b) (Brivio et al., 2013)	16
Figure 6. Octahedral and tolerance factors for various HOIPs (Chen et al., 2015).	17
Figure 7. Schematic diagram of the energy levels of the 18 metal halide perovskites (Tao et al., 2019).....	18
Figure 8. Crystal structure of double perovskite based on titanium (Ju et al., 2018)..	19
Figure 9. the stability of photovoltaic devices based on Cs_2TiBr_6 (Chen et al., 2018). 20	
Figure 10. Calculated band gaps of all double perovskite (Ju et al., 2018).....	21
Figure 11. various diamond anvil geometries and the reported pressure as function of the publication year (O'Bannon III et al., 2018).	22
Figure 12. The schematic diagram of DACs mechanism (a) and a photo of high-pressure in-situ diffraction probes (b) (Lü et al., 2017).....	24
Figure 13. Pressure induced XRD pattern of MAPbBr_3 (a) and MAPbI_3 (b) (Jaffe et al., 2016).....	26
Figure 14. In situ XRD of $\text{Cs}_2\text{AgBiBr}_6$ under compression (a) (Fu et al., 2019) and calculate lattice constant of Cs_2TiBr_6 with various pressure (b) (Liu et al., 2021).	28

Figure 15. Normalized photoluminescence (PL) spectra of MAPbI ₃ as applied pressure (a) (Jaffe et al., 2016) and PL spectra of MAPbBr ₃ as a function of pressure (b) (Wang et al., 2015).....	30
Figure 16. the fluctuation in the band gap of Cs ₂ AgBiBr ₆ as a function of different pressures applied (Li et al., 2017).	31
Figure 17. Calculated band gap of Cs ₂ TiBr ₆ as a function of pressure (a) and calculated absorption coefficient of Cs ₂ TiBr ₆ as a function of pressure (b) (Liu et al., 2021).....	31
Figure 18. Diagram of Energy calculated theoretically with various methods.....	33
Figure 19. Schematic workflow of DFT calculation.	38
Figure 20. Schematic of experimental approach for inverse temperature crystallization (a) and a diamond anvil cells (b)	40
Figure 21. Optical photographs of double perovskite Cs ₂ TiBr ₆ preparation starting from (a) solution synthesis, (b) solution heating, and (c) powder anealing.	41
Figure 22. Diagram of Jablonski presents the fundamental process of Rayleigh, anti-Stokes and Stokes Raman Scattering. (Mosca et al., 2021).....	43
Figure 23. A Comparison between observed and calculated Raman spectra of MAPbI ₃ in the low-frequency range up to 760 cm ⁻¹ . The vertical arrows are guides to the eye and indicate the frequencies of the Raman modes with the highest intensity. The green lines and purple sticks have been obtained from the first-principles calculation through CASTEP codes and QE codes, respectively.	48
Figure 24. The Raman spectra of MAPbI ₃ observed at fingerprint frequency range, while their predictions from CASTEP and QE codes are included for comparison. For clarity, the Raman spectra are measured at ambient pressure and room temperature.	50
Figure 25. Schematic representations of Raman vibrational modes in MAPbI ₃ . The vibrational modes of PbI ₃ framework from top view where Pb atoms in black color and I atoms in grey color (a); and the internal vibrational modes of organic MA from	

side view where C, N, and H are in green, blue, and yellow color, respectively (b-h). The red arrows are the vibrational movements.	53
Figure 26. XRD spectra of the double perovskite Cs_2TiBr_6 powder gained by solution synthesis method.	56
Figure 27. A comparison between observed Raman spectrum of Cs_2TiBr_6 cubic phase $\text{Fm}\bar{3}\text{m}$ with the calculated Raman spectrum by using CASTEP code.	59
Figure 28. Observed Raman spectra from MAPbI_3 upon compression (upper chart) and comparative results of Raman modes by DFT calculation (lower chart).	61
Figure 29. The evolution of Raman shift of MAPbI_3 as a function of pressure across frequency range 50–225 cm^{-1} (a), 480–740 cm^{-1} (b), the schematics of MAPbI_3 perovskite illustrate the vibrational motions including PbI_3 framework stretching modes and internal MA modes under ambient condition (c) and hydrostatic pressure at 3.26 GPa (d).	63
Figure 30. The pressure-induced Raman spectra evolution of MAPbI_3 across fingerprint range where observed data shows on an upper chart and calculated data shows on a lower chart. Inset: Raman shift dication.	67
Figure 31. Raman patterns of double perovskite Cs_2TiBr_6 upon compression up to 20.6 GPa and decompression to ambient pressure.	70
Figure 32. The Raman shift evolution of double perovskite Cs_2TiBr_6 as a function of pressure across frequency range 50–800 cm^{-1}	71
Figure 33. A comparison between observed Raman spectrum of Cs_2TiBr_6 tetragonal phase P4/mnc with the calculated Raman spectrum by using CASTEP code.	72
Figure 34. Total enthalpy as function of pressure (a), cubic phase $\text{Fm}\bar{3}\text{m}$ (b), and tetragonal phase P4/mnc (c).	74
Figure 35. Calculated phonon dispersions and phonon density of states for Cs_2TiBr_6 in tetragonal phase P4/mnc	75

Figure 36. High-pressure photoluminescence properties of Cs_2TiBr_6 . Changes in the PL spectra of Cs_2TiBr_6 with pressure range 0-12.6 GPa (a) and 12.9-20.6 GPa (b). 77

Figure 37. Optical micrographs of Cs_2TiBr_6 in a DAC, showing piezochromic transitions from translucent red to dark black (a). PL peak position (b) and full width at half-maximum (FWHM) (c) as a function of pressure during compression. 79

Figure 38. Pressure-induced emission mechanism associated with STE in Cs_2TiBr_6 . Schematic configuration coordinate of emission for Cs_2TiBr_6 at ambient pressure (a) and high-pressure (b). 81



CHAPTER 1

INTRODUCTION

1.1. Background

Energy is a critical aspect of human life, and its consumption is rising in lockstep with human and industrial expansion. Indeed, worldwide energy consumption will be globally grow by 44 %, or 472 quadrillion Btu, between 2006 and 2030. (EIA, 2021). In recent decades, the solar energy promises great performance for future energy harvesting, since their sustainability, cleanness, and abundance. In comparison to the other energy resource, the solar energy irradiating the earth of 38,500,000 exajoule per year and the electrical conversion disadvantage of fossil fuels is producing high carbon emission (WEC, 2013). Since the worst long-term impact of carbon and the reduced of fossil fuel resource, the research development have been devoted to the solar energy conversion. As the same time, several research of harvesting solar energy rapidly grow. The greatly development of photovoltaic (PV) applications can convert the solar energy into electrical energy. According to the US energy information and administration 2021, the cost per power unit of PV is exponentially decreasing throughout the years. The research development of PV has been carried out in various generations such as silicon solar cells, Copper indium gallium selenide solar cells (CIGS), cadmium telluride solar cells (CdTe), organic solar cells (OSC) or dye-sensitized solar cells (DSSC), and perovskite solar cells. In the end, H. Zhou et al.

presented that the perovskite solar cells (PSCs) become promising sectors that create new leading innovation on PV due to their inexpensive production and the previous report of their efficiency over 22% (Zhou et al., 2014).

The hybrid organic-inorganic perovskite (HOIPs) have become a promising research topic in various photovoltaic and optoelectronic devices due to their high solar absorption, ease of fabrication, low cost, and long carrier diffusion length, with over 3000 publications (Buriak, 2017). The typical HOIPs structure is denoted by the formula ABX_3 , where A, B, and X represent a monovalent organic cation, a metal cation, and a halide anion, respectively (Liang et al., 2017). Previously, the optical and electronic properties of HOIPs were extensively investigated via chemical substitution. HOIPs based on methylammonium (MA/CH_3NH_3) lead iodide (PbI_3) prepared via the inverse-temperature crystallization (ITC) method are capable of exceeding 22% efficiency in power conversion (Alsalloum et al., 2020). In comparison to typical HOIPs, the $MAPbI_3$ has a narrow direct band gap of 1.6 eV and a high absorption coefficient of 280 nm, which is close to the Shockley-Queisser optimum (Shockley & Queisser, 1961). Furthermore, the effective masses of free electron and hole carriers are small, resulting in high mobilities of up to $50 \text{ cm}^2\text{V}^{-1}\text{s}^{-1}$ (Stranks et al., 2013).

It is commonly known that substituting cesium (Cs^+) for MA^+ or other organic cation in HOIPs considerably improves their stability (Z. Li et al., 2016). Additionally, it has been considered that Pb^{2+} may be substituted for with various cations to avoid potential toxic devices, including tin (Sn^{2+}), titanium (Ti^{2+}), germanium (Ge^{2+}), bismuth (Bi^{3+}), antimony (Sb^{3+}), indium (In^+), and silver (Ag^+). The double perovskites based on Cs_2TiBr_6 has recently been identified as a promising candidate in the search for novel Pb-free perovskites, with solar cell efficiencies as high as 3.3% is reported by Min-Chen, et al (Chen et al., 2018). It has bandgap of 1.78 eV and appropriate for use in tandem photovoltaics (Ju et al., 2018). Additionally, the presence of strong photoluminescence indicates a low non-radiative recombination rate, and diffusion lengths greater than 100 nm have been measured.

Previous studies on the electrical and optical characteristics of MAPbI_3 and Cs_2TiBr_6 have been presented (Euvrard et al., 2020; Jaffe et al., 2016). However, the essential understanding about their microscopic activity remains unexplored, for instance, the structural transition and atomic interaction that have a direct impact on device performance. The structural transition is critical for the stability of perovskite materials and has gained immense attentions. Additionally, Pressure enables the modification of the crystal structures of certain materials and leads to altering their optical and electrical characteristics (Jaffe, Lin, & Karunadasa, 2017). Along with structural transitions, pressure can alter the local electronic Fermi surface structure

between the conduction and valence bands, resulting in a narrow conversion of the Fermi level and subsequent metallization (Lijun Zhang et al., 2017).

Several research groups have explored the crystal structures of MAPbI₃ by utilizing X-ray diffraction under high pressure to determine their compositions. Previously, the lattice development of MAPbI₃ under pressure was seen as a tetragonal (*I4/mcm*) α -phase at ambient pressure to a cubic (*Im3*) β -phase at about 0.4 GPa – 2.71 GPa (Jiang et al., 2016; Szafranski & Katrusiak, 2016). Other observations verified that the orthorhombic structure occurs at 0.3 GPa and is followed by a completely amorphous phase at 3 GPa (Capitani et al., 2016). MAPbI₃ has a band-gap of 1.537 eV at ambient pressure. As the pressure is raised, the band gap of MAPbI₃ exhibits a notable red-shift to 1.507 eV at 0.32 GPa, followed by a blue-shift (Kong et al., 2016). Furthermore, the metallic phase of MAPbI₃ has been found to be greater than 60 GPa (Jaffe, Lin, Mao, et al., 2017). In fact, it can be difficult to determine the positions of lighter atoms such as hydrogen, carbon, and nitrogen. On the other hand, Raman spectroscopy, infrared (IR), nuclear magnetic resonance, and neutron scattering have all been employed to investigate phonons and vibrations in the context of their importance to the environment. Based on previously published results, the Raman spectrum range of MAPbI₃ may be divided into three separate regions: the internal vibration of the PbI₆ octahedral framework (0-60 cm⁻¹), the libration and spinning of organic MA (60-180 cm⁻¹), and the internal vibration of organic MA (0-60 cm⁻¹) (180-

3200 cm^{-1}) (Pérez-Osorio et al., 2015). Despite the fact that vibrational modes have been discovered, there is still a lack of knowledge of the pressure-induced Raman vibrational modes, particularly in MAPbI_3 and other materials.

In other hands, the double perovskites as new comer in PV devices have been less explored on the effect of high-pressure for example Sr_2ZnWO_6 achieved a structural transition from a monoclinic phase (P21/n) to a triclinic phase (P1) at a pressure of 9 GPa, followed by an increase in resistivity of more than one order of magnitude (N. Li et al., 2016). The band gap of a developing lead-free photovoltaic perovskite $\text{Cs}_2\text{AgBiBr}_6$ has been narrowed by a significant 22.3%. The band gap of $\text{Cs}_2\text{AgBiBr}_6$ (about 1.7 eV) at 15 GPa is comparable to that of basic photovoltaic perovskites (MAPbI_3) (Li et al., 2017). The $\text{Cs}_2\text{AgBiBr}_6$ is completely changed from cubic to tetragonal between 4.0 and 6.5 GPa. Above 6.5 GPa, structural amorphization of tetragonal $\text{Cs}_2\text{AgBiBr}_6$ occurs (Fu et al., 2019). Moreover, the double perovskite based on Cs_2TiBr_6 has a predicted band gap of 1.81 eV using the Density Functional Theory with Hubbard U correction (DFT + U) technique, which coincides well with the experimental result. When compressed to 15 GPa, the band gap of Cs_2TiBr_6 drops from 1.81 to 1.46 eV (Liu et al., 2021). However, the high-pressure technique is experimentally needed to determine their chemical/physical characteristics, such as pressure-induced bandgap and size-dependent phase transitions.

Therefore, the single crystals of MAPbI_3 and Cs_2TiBr_6 is effectively produced in this study by employing inverse temperature crystallization (ITC). The pressure-induced Raman vibrational of MAPbI_3 is investigated to understand the internal interaction of organic MA and inorganic cation by measuring the Raman spectrum of the crystal. The evolution of Raman vibrational in Cs_2TiBr_6 is also observed to explore the atomic interactions under pressure. The structure transition of Cs_2TiBr_6 is determined using XRD. The diamond anvil cells (DACs) are used in order to create the hydrostatic pressure. DFT calculation is used to conduct a detailed group-theoretical analysis of the Raman activity of each mode during compression, which allowed us to investigate the activity of each mode in more depth, and also to determine the crystal structures as well as the electronic behavior. By studying the vibrational and structure evolution under pressure, we were able to get insight into the relationship between applied pressure and atomic interaction, which may be beneficial for further pressure optimization of MAPbI_3 and Cs_2TiBr_6 .

1.2. Aims of The Research

According to the background and motivations, some goal strategies are pointed out as follows:

1. To prepare and synthesize the hybrid perovskite and double perovskite based on MAPbI_3 and Cs_2TiBr_6 , respectively.

2. To identify the Raman vibrational properties of MAPbI_3 and Cs_2TiBr_6 under high-pressure by employing Raman spectroscopy.
3. To identify the pressure-dependent crystal structure of Cs_2TiBr_6 by using X-ray diffractometer.
4. To observe the optical properties included photoluminescence and absorption of Cs_2TiBr_6 .
5. To theoretically investigate the pressure-induced physical properties (i.e. vibrational modes, structural property, electronic and optical properties) of MAPbI_3 and Cs_2TiBr_6 based on DFT calculations.

1.3. Research Flow

The research began with a desk study and preliminary study, followed by searching for relevant literature on the hybrid perovskites, double perovskites, high pressure technology, and its effect to the physical properties of perovskites. The literature review findings will be used to decide perovskite materials for this study, considered on ease processing, inexpensive and performance in PV devices. The materials preparation and synthesize will be conducted at Semiconductor Physics Research Laboratory (SPRL), department of physics, Chulalongkorn University. After obtaining the samples, the characterization of vibrational properties under pressure will be performed at Extreme Condition Physics Research Laboratory (ECPRL), department of physics, Chulalongkorn University and as well the computational study. The partial

experiment data such as the structure evolution and optical behavior under pressure will be conducted at related laboratory outside University. The data will be gathered, analyzed, and compared between experiment and computational approach. Finally, the data will be discussed and proposed for article in reputed international journal.

1.4. Thesis Structure

The thesis is organized into five chapters. Each of chapters were carried out in several stages and be described in full below:

The first chapter provides an overview of the scientific background, motivation for the study, and the goals of research, specifically hybrid perovskites and double perovskites under high-pressure.

The second chapter provides a literature review regarding to the research work. The majority of the review discusses the perovskites in general, their crystal structure, high-pressure technology and the pressure effect on perovskites.

The third chapter conducts the methodology including the synthesis and characterization of the hybrid perovskites and double perovskites. The detail of high-pressure technique is provided as well. In addition, the computational method is described to support the ideas.

Fourth chapter provides the result and discussion regarding the pressure-induced the phase evolution of hybrid and double perovskite. In addition, the pressure-induced

photoluminescence was presented to understand the mechanism between external pressures with optical properties of perovskite.

Finally, the last chapter presents the conclusions of this work and also give the future research suggestions that can improve this work.



CHAPTER 2

LITERATURE REVIEW

2.1. Photovoltaic (PV)

Photovoltaic (PV) devices generate energy from sunlight by an electrical process that occurs naturally in the presence of a semiconducting substance, which is used in their construction. As a result, the research and development of cost-effective photovoltaic technology is critical to the realization of large-scale solar energy generation in the near future. Liquid ink solar cells, up conversion solar cells, light absorption dyes, quantum dots, organic/polymer solar cells, adaptive cells, and perovskites solar cells are all examples of advanced solar cell research now underway. Among them, the perovskite solar cell continues to be a significant class of emerging photovoltaic technology (Park, 2015). Great news for solar PV is that the cost per unit of energy produced has been declining at an exponential rate over the last few years (Figure 1) (EIA, 2021). The data also illustrates that if we continue on our current path, by 2030, the cost of solar PV will have dropped dramatically, making it the least expensive source of energy when compared to all other forms of energy.

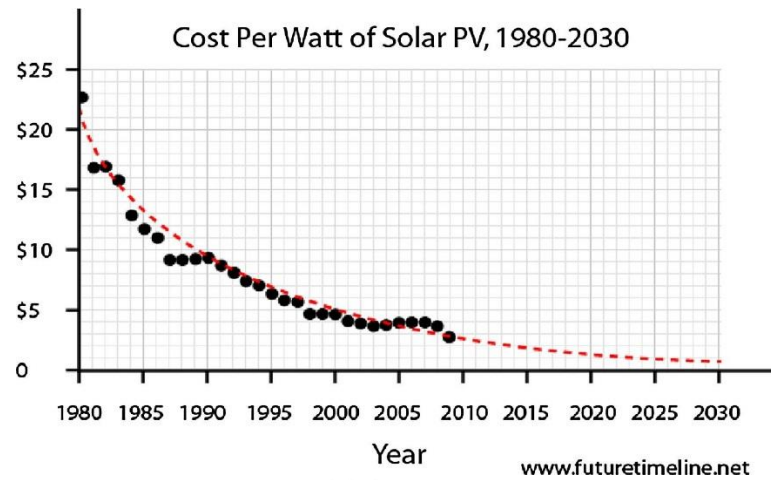


Figure 1. World solar photovoltaic cost through the years (EIA, 2021).

The advancement of solar cell innovation is characterized by a specific end goal: to produce a low-cost, high-efficiency, and long-lifetime solar cell that is a superior alternative to fossil fuels while being cost-effective. The pursuit of novel materials and innovative device techniques in solar cells has been motivated mostly by the aim to fulfill these three goals in photovoltaic technology innovation. Solar cells are divided into four groups as depicted in figure 2, which are based on the historical period in which they first appeared on the market (Balema, 2009). Solar cells that are now available on the market are mostly "Generation I" devices, which are built of crystalline silicon and have a high efficiency (c-Si). They are rather expensive to create, owing to the high processing expenses that are expected to be incurred in the production of silicon wafers with high purity and long-range order.

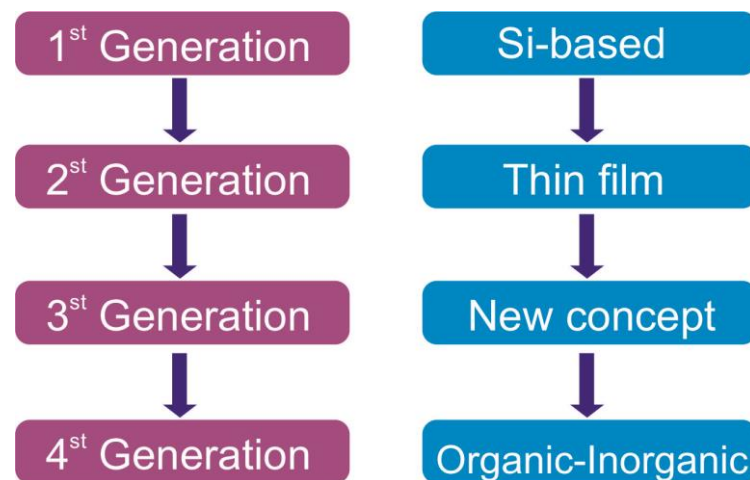


Figure 2. Classification of photovoltaic technology.

Furthermore, because Si-based solar modules are stiff and hefty, they necessitate the construction of costly mechanical support systems. Generation II materials have the least amount of development as a photovoltaic (PV) technology. They are typically deposited using either vacuum-assisted or chemical vapour deposition techniques (CVD). The great majority of the constituent elements in these cells are either in restricted supply, making them more expensive (indium), or they are extremely poisonous (chromium and cadmium). With the introduction of organic materials with photovoltaic capabilities, their ability to be produced at a lower cost and with a higher optical absorption positioned them as a third-generation technology. As an alternative to organic solar cells, dye or semiconductor sensitized solar cells have emerged as a candidate that might have an impact on the next generation of PV technology (DSSCs). During the creation of this generation of solar cells, the concept of "inorganics-in-organics" was utilized. It combines the low cost

and flexibility of polymer (organic material) thin films with the stability of unique inorganic nanostructures with the goal of improving the optoelectronic characteristics of the less expensive thin film photovoltaics (PVs). In order to overcome the real difficulties that the first, second, and third generations of solar cells are facing, this new concept was developed. These difficulties include the high cost of first-generation solar cells, the toxicity of second-generation solar cells, the limited availability of materials for second generation solar cells, and the low efficiency of third generation solar cells.

2.2. Perovskites

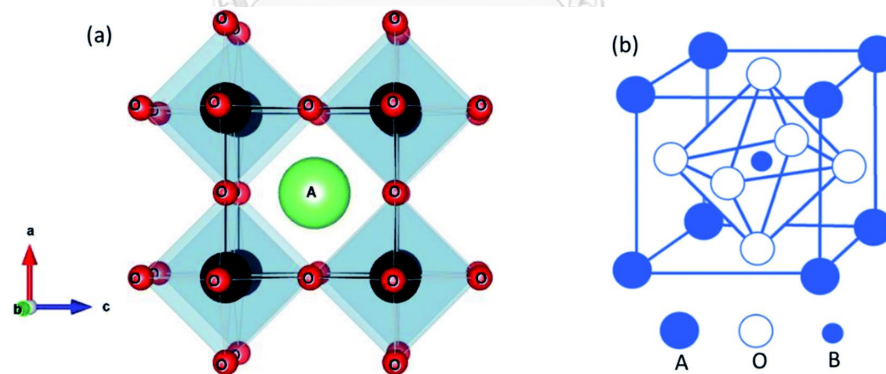


Figure 3. Perovskite structure based ion oxides (Yoshimura & Sardar, 2021)

In 1839, a Russian scientist named Gustav Rose discovered a new mineral which is made of calcium titanium oxide (CaTiO_3). Then, Research was carried out further by the Russian mineralogist Lev Perovski, and as a result, this mineral was given the

name Perovskite. The crystal structure of perovskite (CaTiO_3) is orthorhombic (space group $Pbnm$). There are a large number of compounds with the general formula ABO_3 that have the perovskite structure as seen in figure 3, where A is divalent and B is tetravalent, so that Ca can be partially or completely replaced by Na, Mn, Ce, Sr, Pb, and Ti by Fe, Nb, Zr, and Mg, with the valency accommodated by paired substitution, for example, $\text{Fe}^{3+} + \text{Nb}^{5+}$ replacing Ti^{3+} . Perovskites are a family of materials that have a similar structure and exhibit a wide range of fascinating features such as superconductivity, magnetoresistance, and other properties, among others. This class of readily synthesized materials is often regarded as the solar cell of the future, due to their unique structure, which makes them ideal for allowing low-cost, high-efficiency photovoltaics.

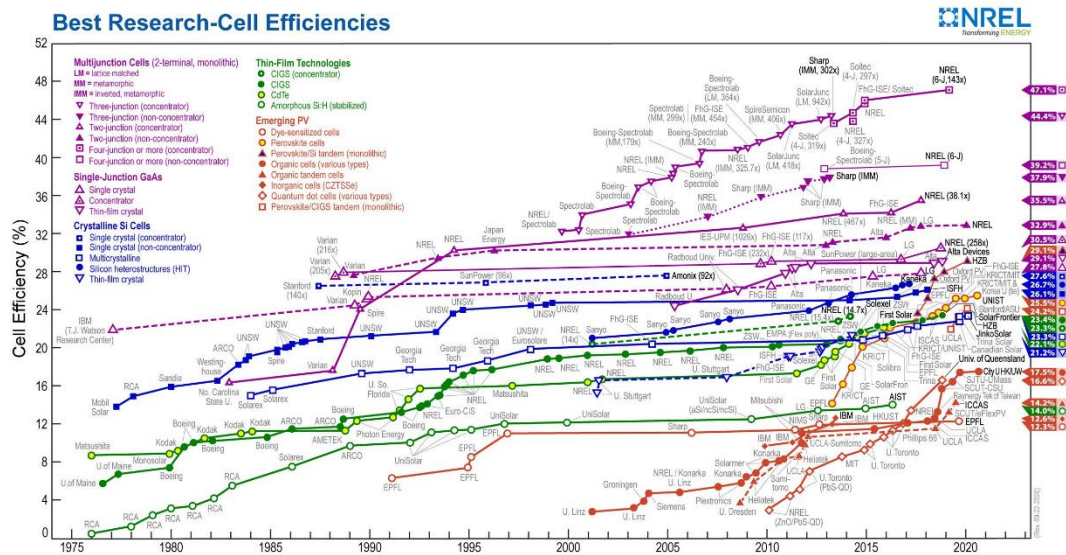


Figure 4. Conversion efficiency of solar cells with various materials (EIA, 2021).

As seen in Figure 4, certified record efficiency as reported by the National Renewable Energy Laboratory (NREL) has already surpassed 22 percent. It can be determined from the record certified efficiency that the PSCs (24.2 percent) currently outperform some mature technologies, such as amorphous Si (14.0 percent), thin film and multi-crystalline Si (21.2 percent and 22.3 percent, respectively), and they are comparable to CdTe (22.9 percent) and CIGS (23.3 percent) cells in terms of efficiency (EIA, 2021).

2.3. Hybrid Organic-Inorganic Perovskites

The use of hybrid organic-inorganic perovskites (HOIPs) solar cells has emerged as the most promising candidate for next generation high efficiency solar cell technology because they are compatible with low-cost, low-temperature processing, flexible substrates, and large-area fabrication using techniques such as ultrasonic spray-coating, printing, roll-to-roll, and vapor deposition. It took just four years to develop laboratory-scale solar cells with the maximum power conversion efficiency (PCE) of 20.1 percent, which is only a few percentage points lower than the best single-crystalline silicon solar cells on the market.

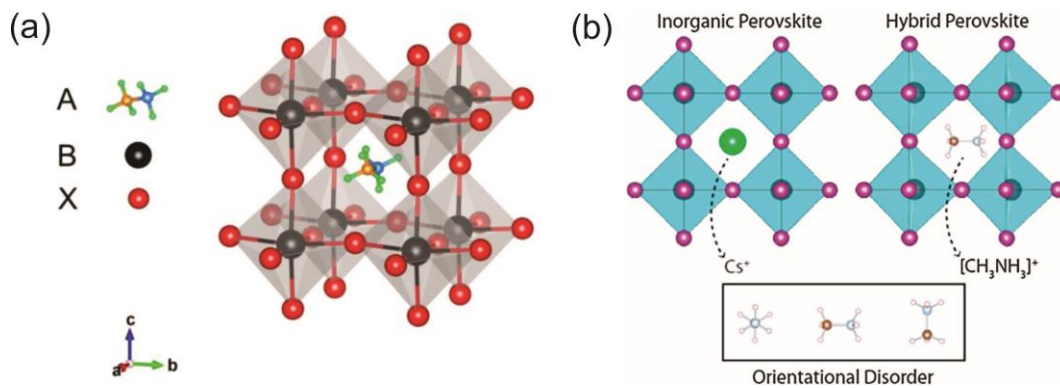


Figure 5. Hybrid organic inorganic perovskite structure (a) (Cho et al., 2021) and the structural differences between Inorganic with hybrid perovskite (b) (Brivio et al., 2013)

Figure 5a. presents that the Inorganic halides (I, Cl, Br) replace the oxygen anion in HOIPs. The halide anion is usually matched by an organic or inorganic monovalent A⁺ cation and a divalent B²⁺ metal cation. The A site is frequently filled by an organic component in hybrid organic–inorganic halide perovskite (hybrid perovskite), which is most typically labeled as CH₃NH₃PbI₃ (MAPbI₃). Halide perovskites, like their parent oxide perovskite, must adhere to tolerance factors in order to attain desirable crystal symmetry. Goldsmith's tolerance factor can be used to monitor perovskite crystal stability and symmetry, as followed:

$$t = (R_A + R_B) / \sqrt{2}(R_B + R_X)$$

and also octahedral factor

$$m = R_B / R_X$$

where R_A , R_B , and R_X are represented the ionic radii of atom A, B, and X, respectively. The stable cubic structure value (t) must be between 0.81 and 1.11. Then for good octahedral value is $0.44 < m < 0.90$. Figure 6 shows a comparison of tolerance and octahedral factors for frequently used halide perovskites.

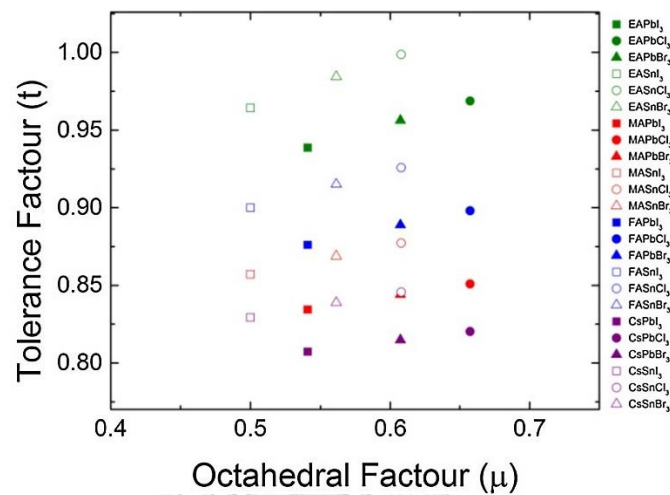


Figure 6. Octahedral and tolerance factors for various HOIPs (Chen et al., 2015).

The methylammonium ion (MA; CH_3NH_3 ; $R_{\text{MA}} = 0.18 \text{ nm}$) is the most widely employed A cation for hybrid perovskites, has reached efficiencies of 15% and higher for MAPbI_3 devices. Due to the tiny size of the MA ion, MAPbI_3 has a tetragonal rather than cubic symmetry at ambient temperature. This results in a bandgap of 1.51–1.55 eV as presented in figure 7, which corresponds to an absorption edge at 820 nm, which is higher than the Shockley–Queisser limit of 1.1–1.4 eV for a single junction solar cell (Pang et al., 2014). Lead (Pb) has shown to be a superior ingredient and it has become the most extensively used of the group IVA metals, accounting for more

than half of all applications. Even though it is poisonous, Pb is still the first option for cation B in today's incredibly efficient PSCs. Pb can be replaced with Sn to produce comparable perovskites with lower and more favorable bandgaps; however, these compounds have lower stabilities because to the ease with which Sn^{2+} can be oxidized to Sn^{4+} . Iodide (I) is the starting material for hybrid perovskites, with the most constant efficiencies about 15% (Umari et al., 2014). Iodide is the most stable structure because it is nearest to Pb on the periodic table and hence shares a comparable covalent nature. While iodide has served as a basis for hybrid perovskite halide components, its susceptibility to oxidation has raised significant concerns about their stability. Thus, iodide replacements and perovskites composed of mixed halides are of significant interest.

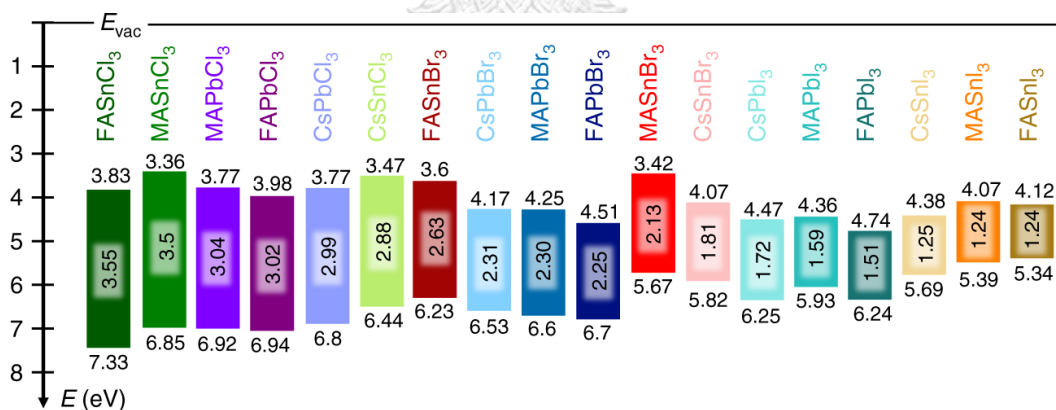


Figure 7. Schematic diagram of the energy levels of the 18 metal halide perovskites

(Tao et al., 2019).

2.4. Double Perovskites

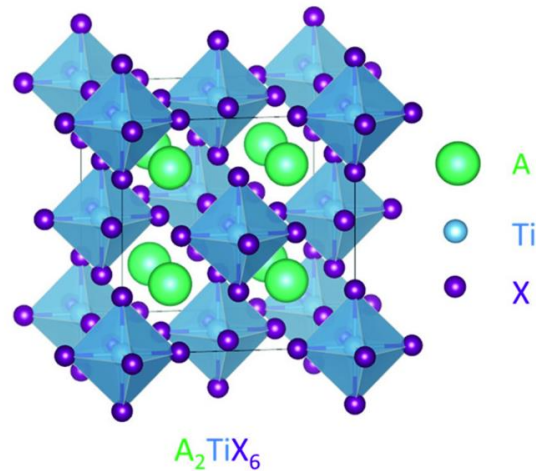


Figure 8. Crystal structure of double perovskite based on titanium (Ju et al., 2018).

Significant effort has been made to develop non-toxic, stable halide perovskites (HP) with photovoltaic and photoelectric capabilities equal to those of Pb-based perovskites. As seen in figure 8, double perovskites with the chemical formula A_2BX_6 (B = tetravalent cation) have been extensively explored, and it might be considered of as a variant of the traditional ABX_3 in which every other B^{2+} cation is absent. Ti has a stable oxidation state of +4, is non-toxic, and contains a high amount of the element earth. Cs_2TiBr_6 has an optical band gap of 1.8 eV, making it an excellent candidate for tandem solar cells due to its large optical band gap (Ju et al., 2018). It was reported for the first time in 2018 that PCE of 3.3 percent was achieved using Cs_2TiBr_6 thin films (Chen et al., 2018). In addition, the applying thermal/moisture stressors to both Cs_2TiBr_6 HP samples demonstrate no gradations compare to hybrid

perovskite as seen in figure 9. These findings show that Ti-based HPs are more stable than Pb-based HPs in terms of reliability. The Ti-based HPs' increased stability is due to their all-inorganic character and the exceptionally stable covalent/ionic interaction between Ti (IV) and halide ions (Ju et al., 2018).

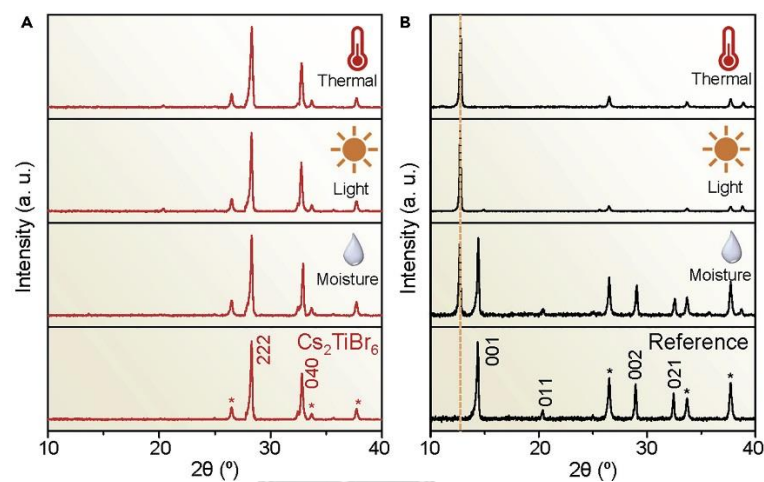


Figure 9. the stability of photovoltaic devices based on Cs_2TiBr_6 (Chen et al., 2018).

These perovskites have three-dimensional (3D) cubic structures with metal halide octahedra sharing corners and a high degree of compositional flexibility, resulting in the formation of the A_2BX_6 double perovskite structure known as elpasolites, which can be used in photovoltaic applications as an alternative method of expanding the perovskite family (Slavney et al., 2016; Zhao et al., 2017). Elpasolites are an unique lead-free perovskite family with a large number of members and more than 350 distinct elpasolites have been synthesized (Giustino & Snaith, 2016). As a result of first-principles calculations, eleven optimum materials with an appropriate bandgap

for use as solar absorbers were discovered. However, these double perovskites have wide band gaps, they cannot be used in single-junction solar cells because of their high band gaps (Liu et al., 2021). For example, the bandgaps of all HPs evaluated in figure 10. As expected, the bandgap grows in the sequence I > Br > Cl, as observed in HOIPs. The bandgap of the Double perovskites widens with increasing A-site cation radius, indicating that the A-site cation's tilting of the $[BX_6]_2^-$ octahedron can significantly impact the electronic structures of these HPs (Stranks et al., 2013).

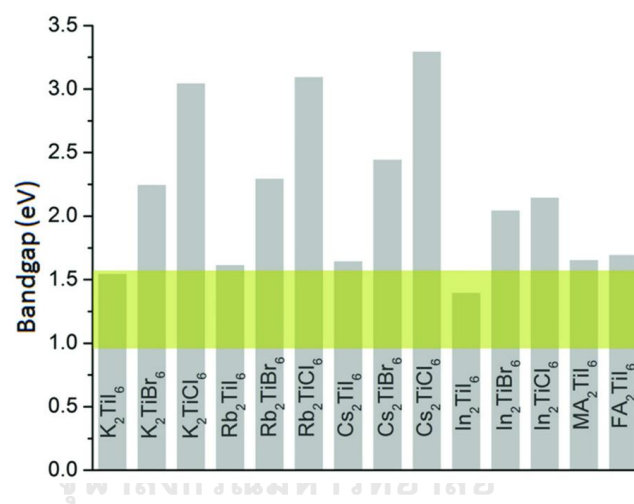


Figure 10. Calculated band gaps of all double perovskite (Ju et al., 2018).

2.5. High-Pressure Technology

Applying mechanical pressure provides a novel method for inducing large changes in optical and electrical behavior, including basic features that are rarely observed under ambient conditions (Lijun Zhang et al., 2017). The employment of high-pressure technologies can result in drastic structural and phase transition changes,

such as lattice disorder, bulk change, cubic distortion, and octahedral tilting. Finally, the pressure can also cause changes in its physical and chemical characteristics such as bandgap closure, tunable photoluminescence, magnetic ordering, metallization, metal-insulator transition, and carrier life time adjustments (Pei & Wang, 2019).

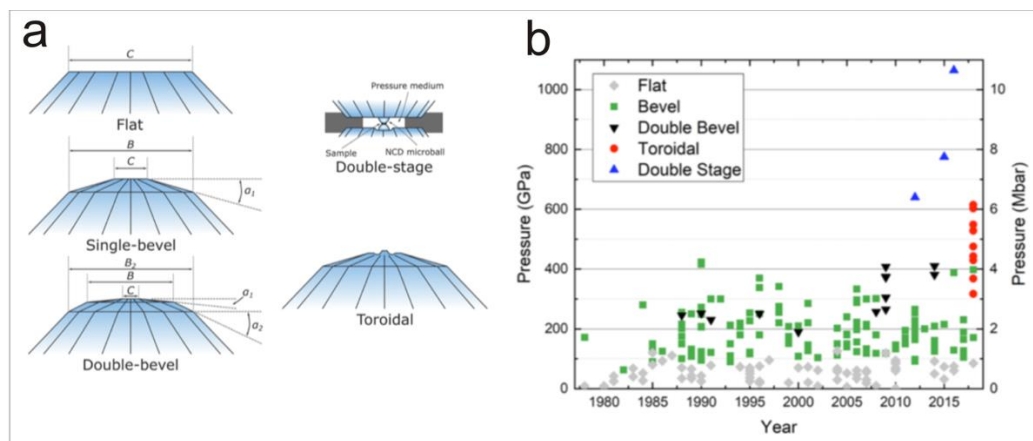


Figure 11. various diamond anvil geometries and the reported pressure as function of the publication year (O'Bannon III et al., 2018).

In order to affecting the properties, as a thermodynamic parameter, the static compression can be employed to perovskite by adjusting bonding patterns, interatomic distance, and electronic orbitals. By using the diamond anvil cells (DAC) as shown in figure 11a, the static compression can be gain up to hundreds giga pascal. The previously utilized pressure range was up to a Terapascal (1000 GPa), also known as megabar pressure. For reference, 100 Gpa (1 Mbar) is the same as 1 million atmospheric pressure found in the earth's core (330-360 GPa) or the maximum pressure found in Jupiter's core (1 TPa) (Alfè et al., 2002).

Figure 11b shows the pressure report as a function of publication year. On multiple stage and flat cullet geometries, the largest and lowest pressures were reported, respectively. For pressures below 400 GPa, a single crystal beveled or double beveled DAC is commonly used (Dubrovinsky et al., 2012). The pressure is also affected by the cullet's diameter. Based on a fit to four data points, Ruoff et al. proposed that the pressure maximum (P_{max}) of DAC is inversely proportional to the square root of cullet diameter (d) (Ruoff et al., 1990).

$$P_{max}(GPa) = 1856d(\mu m)^{-0.5}$$

A pair of diamond anvils are placed in opposing geometry and the sample is placed in the middle with ruby and compressing media such as silicon oil, helium, and neon. The diameter of diamond cullet varies from 100 μm – 700 μm . The ruby is used to calibrate the static compression inside. Diamond is the hardest material structure that provides great transparency to a very wide range of wavelengths of electromagnetic radiation. Therefore, these advantages make the DACs attractive for in situ synchrotron and optical probes (e.g.: XRD, UV-Vis, Raman, and etc.) (Shen et al., 2020). Moreover, the DACs can be used for in situ electrical set up, photocurrent, and magnetic measurements.

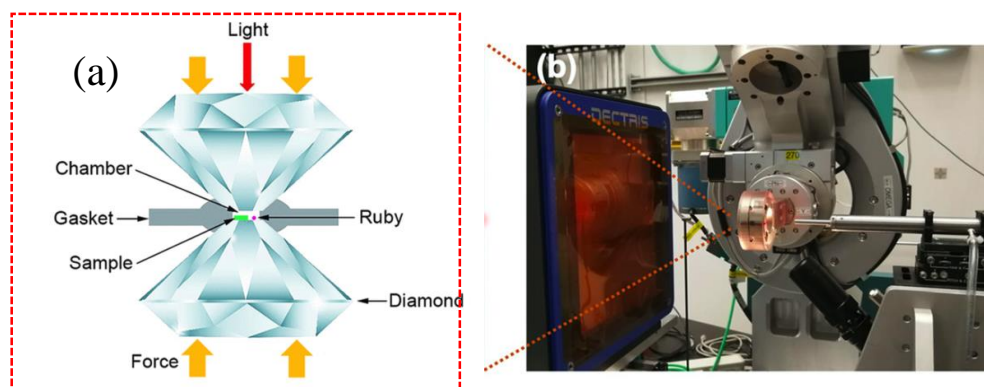


Figure 12. The schematic diagram of DACs mechanism (a) and a photo of high-pressure in-situ diffraction probes (b) (Lü et al., 2017).

Previous study, the high-pressure technology has grown rapidly in physics, chemistry, and materials sciences since it can perform at ambient temperature. It has developed by combining DACs with X-ray diffraction (XRD) and leads to elucidate interesting phenomena. This technique is greatly contributed in various results in evolution of crystal structure, lattice parameters, interatomic length, and bond angle. The phase transition and also changes in chemical bonding can be unveil by using Raman spectroscopy as well. The physical properties of perovskites under high-pressure such as absorption, photoluminescence, and electrical can be monitored by using UV-vis, PL spectroscopy, and electrical measurement set-up, respectively (Jaffe, Lin, & Karunadasa, 2017). Hence, the high-pressure technology can introduce new physical properties related to structure changes, but the reported results might be different one to another due to variable divergent of experimental conditions.

2.6. Structural and Phase Evolution

Perovskites such as MAPbX_3 are the most popular subjects for high-pressure study because of their outstanding performance in energy-related applications and improved chemical stability, making them the most promising candidates. The most investigated aspect of hybrid perovskites under high pressure is structural phase transitions. Given the ephemeral nature of organic-inorganic hybrid frameworks, their lattice structures should be very susceptible to external influences. MAPbBr_3 crystallizes in a $\text{Pm}\bar{3}\text{m}$ cubic structure under ambient circumstances, whereas MAPbI_3 crystallizes in a variety of tetragonal or orthorhombic structures with space groups of $I4\text{cm}$, $I4/\text{mcm}$, and Fmmm (Jaffe, Lin, & Karunadasa, 2017; Jiang et al., 2016). Jaffe et al. used powder and single-crystal XRD studies of MAPbBr_3 and MAPbI_3 to further understand the pressure-induced structural changes. The authors characterized the ambient pressure phase as Tetragonal (α), the second phase under high pressure as cubic (β), and the third phase as amorphous (γ). All of the Pb-X-Pb angles in the structure of the ambient pressure phase of MAPbX_3 are 180° . At certain pressure, the Pb-X bonds tended to shorten, and octahedral tilting occurred at the critical pressure for the phase transition, generating a cubic $\text{Im}\bar{3}$ phase. The volume significantly reduced as following octahedral tilting and bond contraction in the phase- β . Figure 13a presents the pressure-induced amorphization happened in MAPbBr_3 when the pressure exceeded 2.7 GPa, resulting in the creation of the

amorphous γ phase. For MAPbI_3 (figure 13b), the phase achieved in the α - β transition to create an $\text{Im}\bar{3}$ phase when compressed to 0.3 GPa and amorphization began at pressures above 2.9 GPa. Up to the greatest pressure applied, the amorphous phase remained stable with additional compression. Both materials return to their original phase with very little hysteresis when they are decompressed.

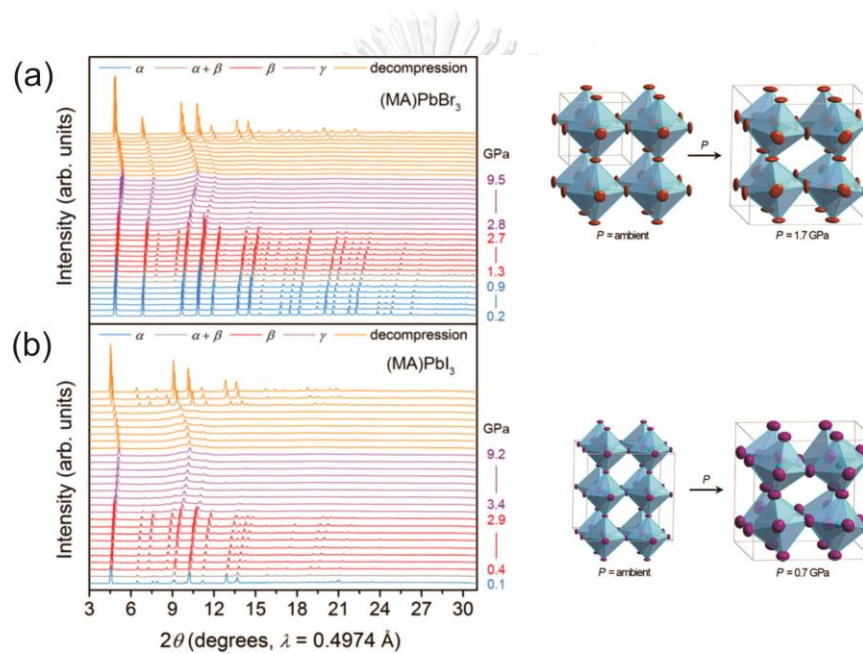


Figure 13. Pressure induced XRD pattern of MAPbBr_3 (a) and MAPbI_3 (b) (Jaffe et al., 2016)

Aside from MAPbX_3 , the double perovskites A_2BX_6 like $\text{Cs}_2\text{AgBiBr}_6$ and Cs_2TiBr_6 have also been investigated for photovoltaic and optoelectronic applications. The inorganic cation (B site) has a big impact on the lattice and electronic structure,

whereas the organic cation (A site) has a big impact on the dielectric constants, hydrogen bonding (between the organic cation and the halide anions), and octahedral distortion. The findings of angle-dispersive synchrotron X-ray diffraction (ADXRD) experiments show that at 2.3 GPa, $\text{Cs}_2\text{AgBiBr}_6$ nanocrystals (NCs) shift from a cubic to a tetragonal structure as seen in figure 14a. A new diffraction peak formed that corresponding to phase II, which could be plainly seen at 3.9 GPa as pressure raised. The high-pressure phase II is a tetragonal phase with the $I4/m$ space group. Only a few wide diffraction peaks were caught when the pressure reached roughly 20.0 GPa, showing that crystallinity is decreasing and $\text{Cs}_2\text{AgBiBr}_6$ NCs have tendency to be amorphous at high pressure. Cs_2TiBr_6 has a calculated lattice constant of 11.10 Å, and when the lattice parameters (a/a_0) ratio is reduced to 0.86, the lattice constant reduces due to the pressure change as presented in figure 14. However, the computational data shows that the imaginary phonon mode of Cs_2TiBr_6 is not exists in the maximum pressure of 15 GPa (Liu et al., 2021).

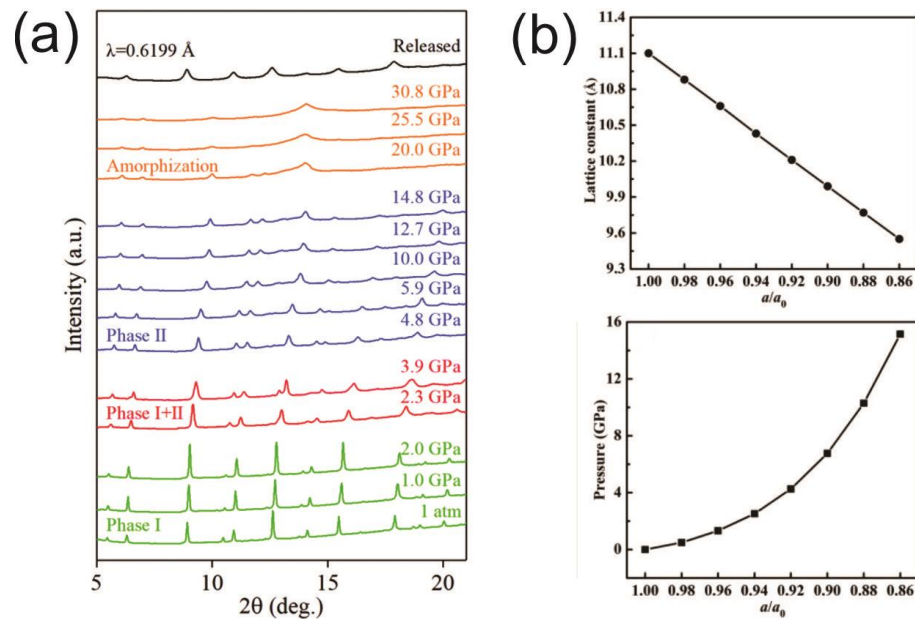


Figure 14. In situ XRD of $\text{Cs}_2\text{AgBiBr}_6$ under compression (a) (Fu et al., 2019) and calculate lattice constant of Cs_2TiBr_6 with various pressure (b) (Liu et al., 2021).

2.7. Electronic and Physical Evolution

Pressure is an alternate method of tuning electronic characteristics, which enables the exploration of novel physical properties and the discovery of new materials with unique behavior. The PL spectra of a single crystal of MAPbI_3 obtained during compression from ambient conditions to 3.1 GPa are shown in the figure 15a. At increasing pressures, PL intensities grow and exhibit a strong correlation with the structural evolution that found in high-pressure diffraction experiments. Pb-I bond contraction implies higher orbital overlap and hence increased band dispersion and decreased bandgap (Jaffe et al., 2016). Whereas, the PL energy undergoes a

significant blueshift, coinciding with the commencement of enhanced octahedral tilting. Further phase compression results in a greater redshift of the PL band from 0.9 to 2.7 GPa, demonstrating that Pb-I bond contraction has a greater influence on the electronic structure. Similar behavior as seen in figure 15b, The bandgap of MAPbBr₃ shifted from red to blue below 1 GPa and then back to red at higher pressures. With increasing pressure, the PL peaks became weaker and eventually invisible due to the amorphous phase (Wang et al., 2015). The sample recovered emission signals upon decompression to atmospheric pressure, accompanied by recrystallization to the original perovskite structure.

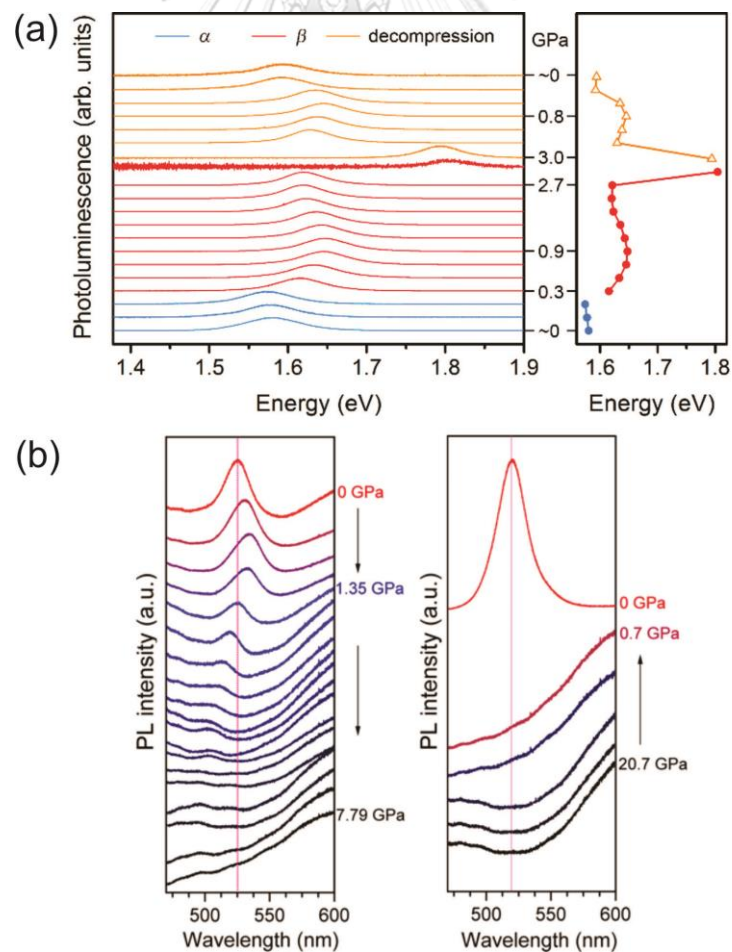


Figure 15. Normalized photoluminescence (PL) spectra of MAPbI_3 as applied pressure (a) (Jaffe et al., 2016) and PL spectra of MAPbBr_3 as a function of pressure (b) (Wang et al., 2015)

In high pressure $\text{Cs}_2\text{AgBiBr}_6$, the Bi-Br-Ag bond angle decreases from 180° to 166.4° solely in the ab plane, whereas the Bi-Br-Ag bond angle along the c axis remains 180° . This reduced octahedral tilting of $\text{Cs}_2\text{AgBiBr}_6$ is thought to be a significant cause in its persistent band gap reduction across a high-pressure range (Li et al., 2017). At 6.5 GPa, structural amorphization of tetragonal $\text{Cs}_2\text{AgBiBr}_6$ effectively generates a massive band gap narrowing from 2.3 to 1.7 eV as presented in figure 16. $\text{Cs}_2\text{AgBiBr}_6$ shows more fascinating band gap behavior at high pressure when compared to lead halide perovskites and around 22.3% of the band gap reduction.

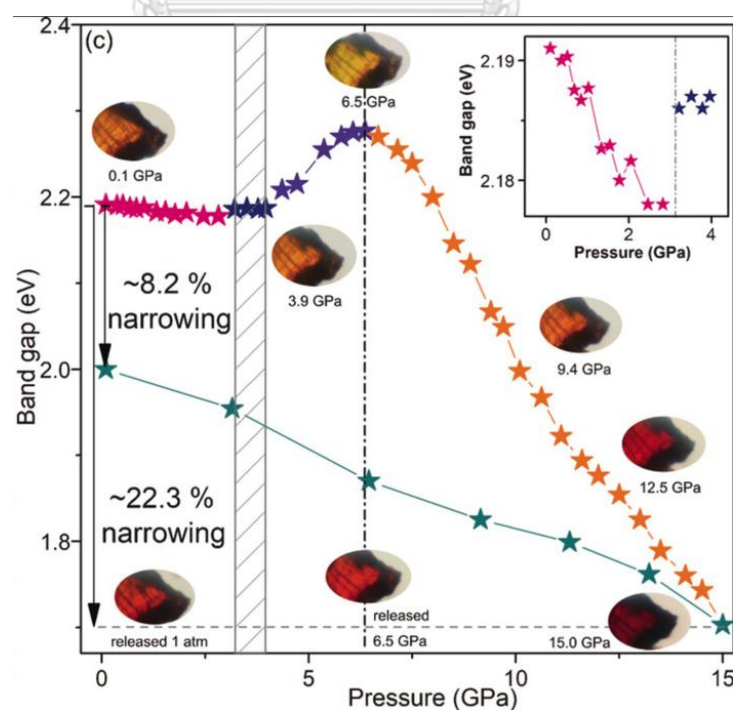


Figure 16. the fluctuation in the band gap of $Cs_2AgBiBr_6$ as a function of different pressures applied (Li et al., 2017).

When the pressure on Cs_2TiBr_6 is increased, the band gap of the material decreases. Using 1.32 GPa as the pressure constant, the band gap of Cs_2TiBr_6 is 1.73 eV, which is similar to the band gap of $CsPbI_3$ (Eperon et al., 2015). The absorption coefficient of Cs_2TiBr_6 is $3.5 \times 10^5 \text{ cm}^{-1}$, which is the highest value. The optical absorption spectra of Cs_2TiBr_6 are shown in figure 17. It can plainly be seen that applying pressure on Cs_2TiBr_6 significantly increases the optical absorption of the compound, which may be attributed to the reduced band gap of the compound. The capacity to absorb light appears to be improved in the wavelength range of 500–800 nm. At 15 GPa, the absorption coefficient of Cs_2TiBr_6 reaches over $4 \times 10^5 \text{ cm}^{-1}$.

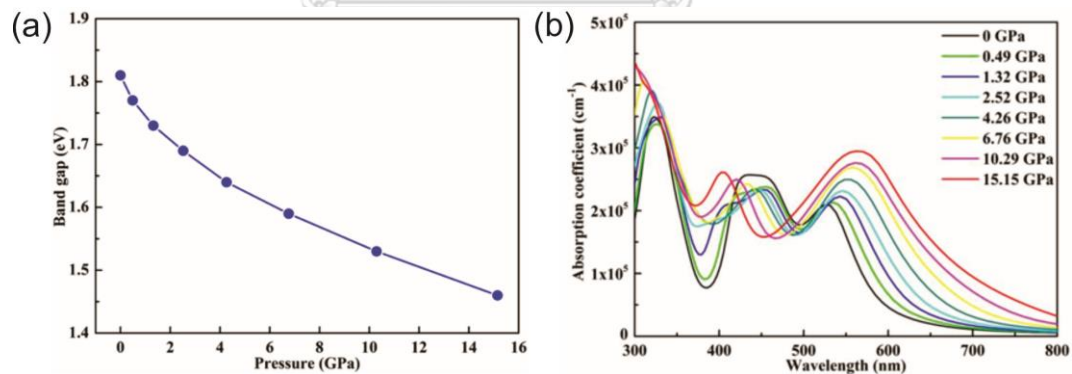


Figure 17. Calculated band gap of Cs_2TiBr_6 as a function of pressure (a) and calculated absorption coefficient of Cs_2TiBr_6 as a function of pressure (b) (Liu et al., 2021)

2.8. Density Functional Theory

At the beginning of Schrodinger's equation, we can predict the behavior of particle in the microscopic world. The Schrodinger depended time equation in Hartree atomic units is written as:

$$\hat{H}\Psi(r_1, r_2, \dots, r_n, R_1, R_2, \dots, R_N) = E\Psi(r_1, r_2, \dots, r_n, R_1, R_2, \dots, R_N) \quad (2.1)$$

Where \hat{H} is the Hamiltonian operator where:

$$H = -\frac{1}{2}\sum_{i=1}^n \nabla_i^2 - \frac{1}{2}\sum_{i=1}^N \frac{1}{M_i} \nabla_i^2 - \sum_{i,I} \frac{Z_I}{|r_i - R_I|} + \frac{1}{2}\sum_{i \neq j} \frac{1}{|r_i - r_j|} + \frac{1}{2}\sum_{i \neq j} \frac{Z_i Z_j}{|R_i - R_j|} \quad (2.2)$$

From the right to the left, respectively, the electrons kinetic energy, the nuclei kinetic energy, Coulomb interactions between electrons and nuclei, Coulomb interactions between electrons and electrons, and Coulomb interactions between nuclei and nuclei are all types of interactions. It's easier to forget about the nuclei's kinetic term in Eq. (2.2) because their weight is 103 times that of an electron, which makes them stay in the same place in space as moving electrons [22]. There is also the coulomb interaction between nuclei and other nuclei term, which can be taken as a fixed number. That makes things easier to understand. There are other ways to approximate the electron system only. This called Hartree approximation where we assumed the ions moving very slowly. So, we can reduce the interaction of ions.

$$\hat{H}\Psi(r_1, r_2, \dots, r_n) = E\Psi(r_1, r_2, \dots, r_n) \quad (2.3)$$

Where, the Hamiltonian of the electron system:

$$H = -\frac{1}{2}\sum_{i=1}^n \nabla_i^2 - \sum_{i,l} \frac{Z_l}{|r_i - R_l|} + \frac{1}{2}\sum_{i \neq j} \frac{1}{|r_i - r_j|} \quad (2.4)$$

However, the energy is still overestimation to the exact ground state energy. Then previously, researcher using Hartree-fock where the only can approximate nearly the exact ground state by following Paulis exclusion where the electron cannot fill the same state.

$$\psi_{HF} = \frac{1}{\sqrt{N!}} \det[\psi_1(R_1)\psi_2(R_2) \dots \psi_{Ne}(R_{Ne})] \quad (2.5)$$

So we can get the exchange and correlation energy between them. Figure 18 shows that in order to reach the system of ground state energy.

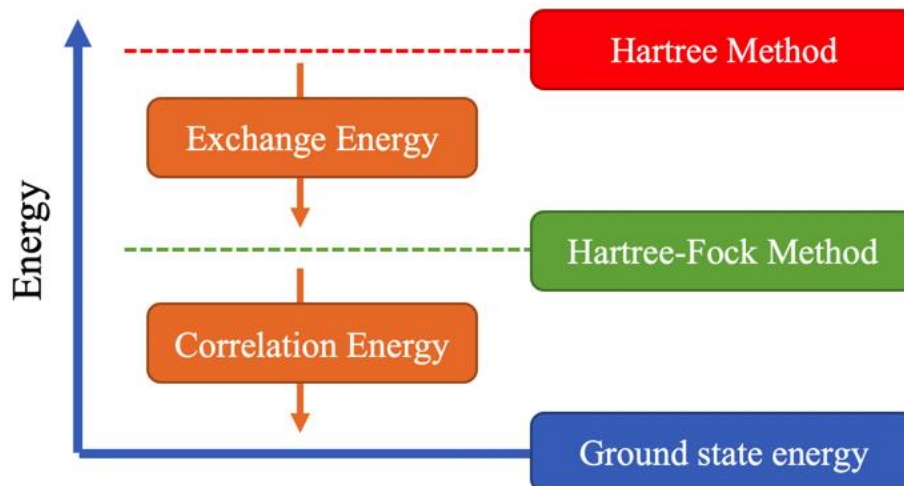


Figure 18. Diagram of Energy calculated theoretically with various methods.

3n-schrodinger equations need to be solved and electron-electron interaction terms in Eq. (2.4) are too complicated to solve. These methods use too many computational resources and can't be solved because they take too long to solve. There are a lot of electron problems that need to be solved, and the density functional theory is what we need to help us figure them out.

Hohenberg and Kohn introduced density functional theory (DFT) in 1964 is a method for computing electron densities. Thus, rather of calculating 3n-dimensional electronic wave functions, the ground state energy of the system is determined using the 3-dimensional electron density, which simplifies the problem while retaining the necessary corrections. Hohenberg and Kohn established two fundamental theorems guiding DFT computations.

2.8.1. Hohenberg-Kohn Theorems

According to the first Hohenberg-Kohn theorem, "the ground state of any interacting many particle system is a unique functional of the electron density $n(\mathbf{r})'$ with a given fixed inter-particle interaction." This suggests that Equation below can be reversed, resulting in the ground state wave function being written as a special functional of the ground state electron density, i.e. $\psi_0 = \psi[n_0]$. In order to represent the ground state energy E as a functional of the ground state density as given in Equation below:

$$E[\psi[n_0]] = \psi[n_0]|\hat{T} + \hat{V} + \hat{U}|\psi[n_0] \quad (2.6)$$

The first Hohenberg-Kohn theorem formally establishes the existence of a functional of the electron density $E[n_0]$, but it makes no mention of the functional's precise form. According to the second Hohenberg-Kohn theorem, the actual electron density corresponding to the complete solutions of the Schrödinger equation is "the electron density that minimizes the energy of the overall functional". In order to determine the ground state electron density, one can try to minimize the energy by altering the electron density if the actual functional form is known. All the properties are calculable once the ground state electron density is known.

2.8.2. Self-consistent Kohn-Sham Equation

The Kohn-Sham equation can be derived from applying the variational theorem as written:

$$\frac{\delta J[n_0]}{\delta n_0} = J_0 \iint \frac{n_0(r')}{|r-r'|} dr' \quad (2.7)$$

and

$$\frac{\delta E_{XC}[n_0]}{\delta n_0} = VXC(r) \quad (2.8)$$

By applying derivative of each variational term, it can be written:

$$\lambda = V_{eff}(r) + \frac{\delta \langle T | n_0 | ref \rangle}{\delta n_0} \quad (2.9)$$

Where, effective potential can be followed:

$$V_{eff}(r) = VNe(r) + \frac{\delta J[n_0]}{\delta n_0} + \frac{\delta E_{XC}[n_0]}{\delta n_0} \quad (2.10)$$

According to the Honhenberg-Kohn theorem, the Kohn-Sham equation as density parameter can be used for calculating all observables. We can apply the electron density $n(r)$ to find the energy functional that given as:

$$\varepsilon_0[n(r)] = T_0[n(r)] + \frac{1}{2} \iint \frac{n_0(r')}{|r-r'|} drdr' + \int [V_{ext}(r)]n(r)dr + E_{XC}[n(r)] \quad (2.11)$$

Form the right to left, respectively, non-interacting kinetic energy functional, electron interaction as known as Hartree energy, and the external potential energy by nuclei.

For non-interacting reference the Hamiltonian operator can be followed:

$$h_i^{KS} = -\frac{\hbar^2}{2m_e} \nabla_i^2 + V_{ref}(r_i) \quad (2.12)$$

And for eigen functions:

$$h_i^{KS} \Psi_m^{KS}(r_i) = \varepsilon_m^{KS} \Psi_m^{KS}(r_i) \quad (2.13)$$

Therefore, the Kohn-Sham orbital in atomic unit can be given by:

$$\left[-\frac{\hbar^2}{2m_e} \nabla_i^2 + VNe(r) + J_0 \iint \frac{n_0(r')}{|r-r'|} dr' + VXC(r) \right] \Psi_m^{KS}(r_i) = \varepsilon_m^{KS} \Psi_m^{KS}(r_i) \quad (2.17)$$

However, the exchange-correlation potential $V_{XC}(r)$ is still unknown information of quantum mechanical and explicit many-body effects. So, it must be modelled by the conventional exchange-correlation functions for instance Local Density Approximation (LDA) and the Generalized Gradient Approximation (GGA). For the whole step process of DFT can be seen in figure 19.



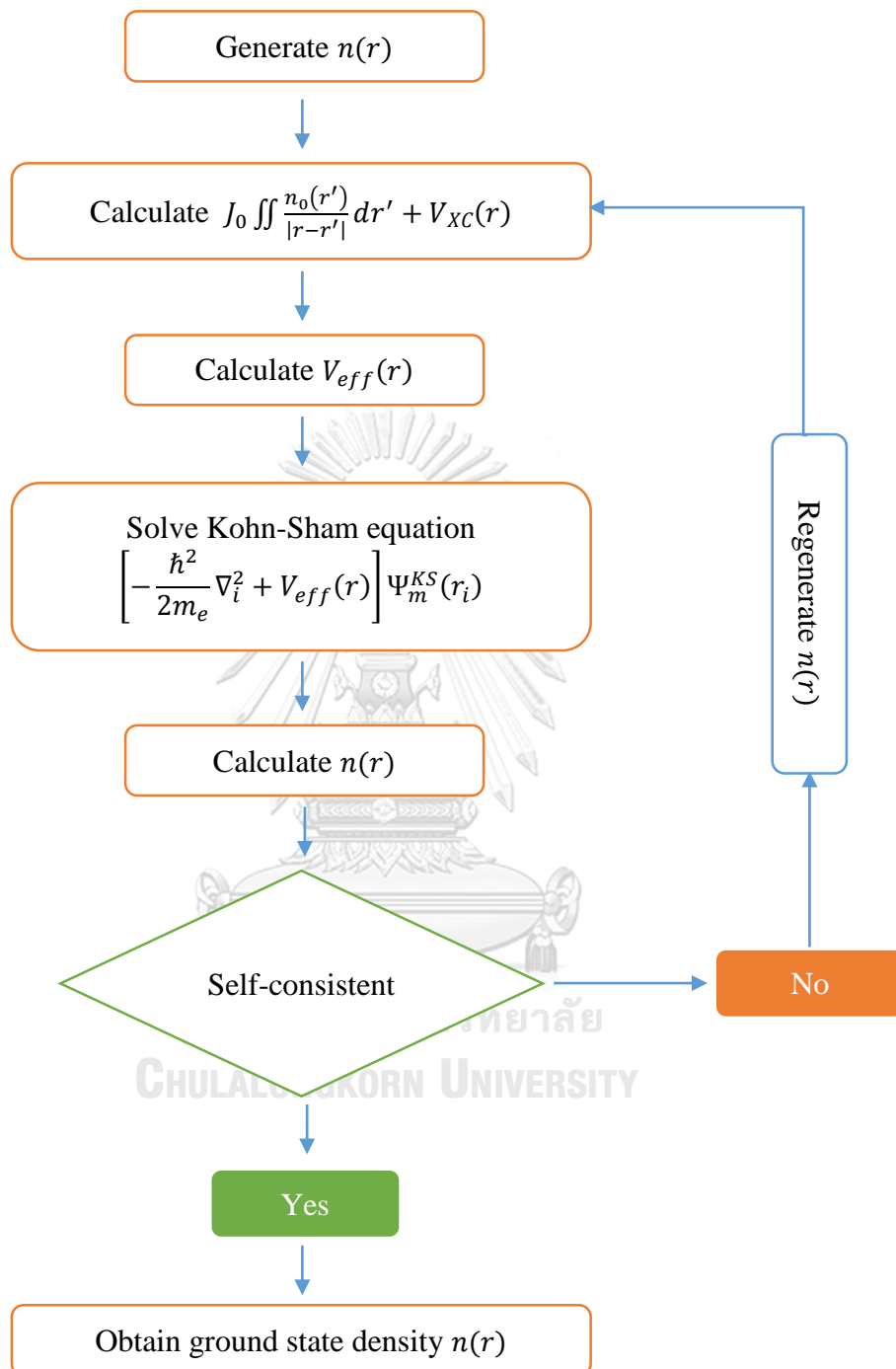


Figure 19. Schematic workflow of DFT calculation.

CHAPTER 3

RESEARCH FRAMEWORK

3.1. Materials Preparation

3.1.1. MAPbI₃ Single Crystal

Methyl Ammonium Iodide (MAI, 99% purity) and Lead Iodide (PbI₂, 99% purity) powders are supplied from Sigma Aldric. and γ -butyrolactone (GBL, 99% purity) are also purchased from Sigma Aldric and used as a solvent without further purification. The single crystal of MAPbI₃ used in this study is grown through inverse temperature crystallization (ITC), as described before (Saidaminov et al., 2015; Zhang et al., 2018). Figure 20 shows a schematic procedure of ITC for MAPbI₃ single crystal. The MAPbI₃ is produced in a 1:1 molar ratio reaction between MAI (CH₃NH₃I) and PbI₂. In a vacuum room with a nitrogen environment and a 10% humidity maintained, the GBL will dropwise to MAPbI₃ mixed powders. The solution compounds will continually dissolve and stirre on a magnetic hot plate at 70 °C until a yellow saturated solution is obtained. The resulting solution will put in an oil bath and gradually heated from 60 °C to 120 °C at a pace of 10 °C per hour. For 5 hours, huge size crystals of black color with a diameter of 1 mm is formed.

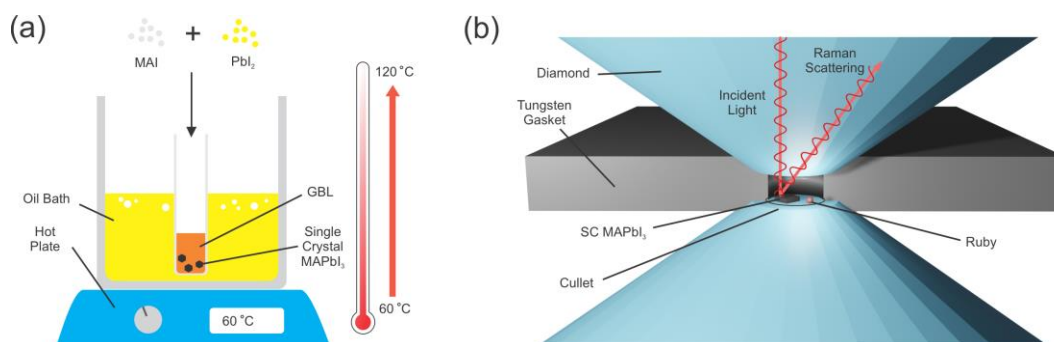


Figure 20. Schematic of experimental approach for inverse temperature crystallization (a) and a diamond anvil cells (b)

3.1.2. Cs₂TiBr₆ Single Crystal

Cesium bromide (CsBr 99.9% trace metals basis), titanium bromide (TiBr₃, 99% purity), and dimethylformamide (DMF, 99.8%) will be purchased from Sigma-Aldrich. Cs₂TiBr₆ single crystal will synthesize via solution synthesis method similar to reported procedures. Solid CsBr (0.426 g, 2.00 mmol) and TiBr₃ (0.449 g, 1.00 mmol) will dissolve in 1 mL of HBr. The detail preparation of Cs₂TiBr₆ can be seen in figure 21. The vial will be capped and heated to 80 °C and continue we stirred the solution around 5-6 hours to get the homogenous solution. Then the solution was poured onto petri glass to remove the solvent at least 30 mins then continue annealed for 30 mins. Finally we got red powder of double perovskite (Euvrard et al., 2020).

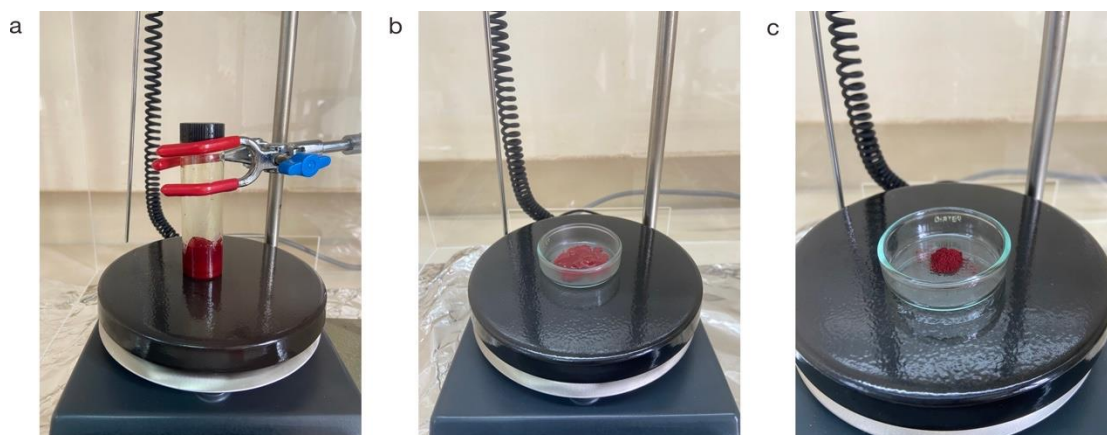


Figure 21. Optical photographs of double perovskite Cs_2TiBr_6 preparation starting from (a) solution synthesis, (b) solution heating, and (c) powder annealing.

3.2. Experimental Method

3.2.1. High Pressure Technique

By using the diamond anvil cells (DAC) as shown in figure 20b, the hydrostatic compression can be gained up to 10 GPa. A pair of diamond anvils will be placed opposing geometry and the both samples is placed inside gasket hole together with ruby sphere and silicone oil as pressure transmitting medium. In order to calibrate the hydrostatic compression inside DAC, a ruby sphere will be placed together with specimen. The diameter of diamond culet and gasket hole is defined of 100 μm and 50 μm , respectively, to ensure desired pressure up to 5 GPa. In particularly, the diamond is the hardest material structure that provides great transparency to a very wide range wavelength of electromagnetic radiation. Therefore, those advantages

make the DACs became attractive for in situ synchrotron and optical probes (e.g.: XRD, UV-Vis, Raman, and etc.).

In our work, the Raman spectroscopy (Horiba, iHR 550) will be used to determine the Raman vibration mode of MAPbI_3 and also Cs_2TiBr_6 . The Raman spectra will be recorded in frequency range of $60\text{-}1500\text{ cm}^{-1}$ under pressure. The spectra will be recorded by monochromator gratings of 1800 lines/mm at room temperature and detected by a TE-cooled Synapse charge couple device (CCD) system. High-pressure Raman studies will be carried using 532 nm line from diode laser as excitation source. Furthermore, the laser beam will be focused onto the samples with the magnification lens of x10. The scattered radiation will be collected in the backscattering geometry with the acquisition time of 30-60 s and accumulation of 10 times. To avoid background light signals, the Raman experiment will be performed in the dark.

3.2.2. The Fundamentals of Raman Spectroscopy

The Raman effects was discovered after Sir. C.V. Raman was returning briefly from London to Bombay by boat and he saw the deep blue sea which was very attractive. At that time, Raman realized that this phenomenon was the result of scattering of sunlight hitting seawater molecules. On the other hand, Rayleigh also observed the blue color of the sky from the scattering sunlight. Regarding air molecules. Raman eventually became obsessed with light scattering and continued his research in

Calcutta. Finally, he got his first journal in the Indian Journal of Physics on 1928. Two years later he was named the Nobel Prize in Physics, 1930 (Monroy et al., 2022).

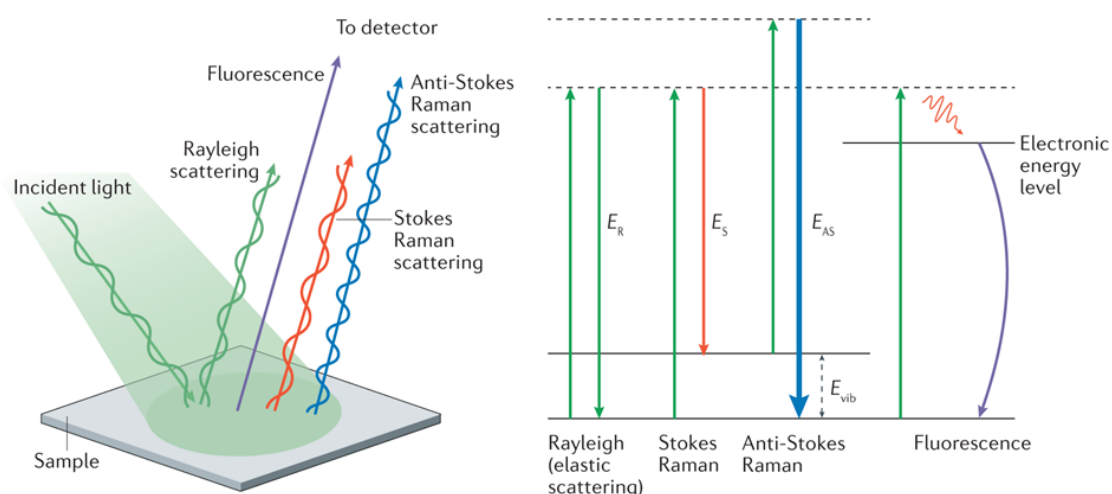


Figure 22. Diagram of Jablonski presents the fundamental process of Rayleigh, anti-Stokes and Stokes Raman Scattering. (Mosca et al., 2021)

His observations found that the light scattered by molecules, whether solid, liquid or gas, has the same wavelength as the incident light. However, it is accompanied by a modified scattering with a different energy value from the incident light (Raman & Krishnan, 1928). The fundamental process of scattering is presented in Figure 1. In the majority of scattering events, the energy of scattering is unchanged after interaction with the incident light, therefore the energy of scattered photon is equal to the incident photon and it is called elastic or Rayleigh scattering. If the scattered photon of molecule loses the energy and the scattered energy less than energy of incident light, it is called Stokes Raman. In contrary, the energy of scattering more than the energy of incident light which can be called Anti-Stokes Raman.

From the above, it is obvious that the wavelength of the excitation light will affect the wavelength of the Raman scattered light. As a result, it is impossible to use the Raman scatter wavelength to compare spectra obtained using various lasers. Thus, a Raman shift away from the excitation wavelength is created from the Raman scatter position as following equation below:

$$\Delta\bar{\nu} = \left(\frac{1}{\lambda_0} - \frac{1}{\lambda_1} \right)$$

The previous formula can explicitly scale for this unit conversion, as provide:

$$\Delta\bar{\nu} (cm^{-1}) = \left(\frac{1}{\lambda_0(nm)} - \frac{1}{\lambda_1(nm)} \right) \times \frac{10^7 nm}{cm}$$

3.3. Computational Method

We will also perform the first-principles DFT calculation as implemented in the Quantum ESPRESSO (QE) package. For generalized gradient approximation (GGA) of Perdew-Burke-Ernzerhof (PBE) was employed to the QE code. In addition, the implementation of projector augmented-wave (PAW) pseudopotentials were generated for atomic compositions as follow: 1 for Pb (5d106s26p2), 3 for I (5s25p5), 1 for C (2s22p2), 1 for N (2s22p3), and 6 for H (1s1). The plane-wave basis sets with converged energy cut-offs of 80 Ry, were verified for all calculations to optimize the structure geometry of unit cells. The k-point Monkhorst-Packs scheme of 8x8x8 was gridded for Brillouin zone integration. In order to search Raman vibrational modes of

MAPbI₃, However, for the second order derivative, it cannot be calculated by DFT only and its requires the perturbation theory. Then, the phonon calculation was used in order to obtain the Raman mode. The phonon calculations were carried out with Density Functional Perturbation Theory (DPFT) using the same set of DFT parameters. At first, we determined the dynamical matrices at Γ point with the phonon threshold of 1×10^{-15} . Then, the eigenmodes and frequencies were obtained by calculated from interatomic force constant in real space. In order to compare the DPFT calculation by QE, we also performed the DFT calculation based on CASTEP code as comparison.



CHAPTER 4

RESULT AND DISCUSSION

4.1. Hybrid Organic-Inorganic Perovskites

In this work, Raman spectroscopy is used to verify the correct composition of the synthesized material in which each atomic bond can be represented by a peak at a certain frequency (Long Zhang et al., 2017). Furthermore, Raman spectroscopy in this case is needed to determine the interactions and relationships between atoms in perovskite materials (Yin et al., 2018). This interaction is a vibration generated by the phonon as a result of the given external light. Usually, the vibrational frequencies in atomic bonds are divided into two regions, namely the low-frequency range (60–760 cm^{-1}) and the fingerprint frequency range (900–1500 cm^{-1}). The low-frequency range usually shows the vibrations of atoms that have a larger mass in this case Pb, Ti, and Cs atoms, while the fingerprint frequency range shows the vibrations of atoms with smaller masses such as hydrogen, carbon, nitrogen, and halide bonds (I and Br). In addition, X-Ray Diffraction (XRD) was also used to determine the phase structure of the perovskite. It should be emphasized that the initial observations using both Raman and XRD were carried out at room temperature. The rest, to support the results of the two experiments, computational methods based on DFT calculations are also used. The results and discussion we describe in the next point.

Figure 22 shows the results of Raman spectroscopy in the low frequency area which was observed to have several peaks of heavy atomic bonds such as lead with iodine. As with previous work, the vibration of the lead-iodine (PbI_3) bond was shown at an initial peak of about 41.6 cm^{-1} (Pérez-Osorio et al., 2015). This peak is so high and large that it covers most of the surrounding peaks. The next peak shows roto-translational vibrations of organic MA molecules around 153.30 cm^{-1} , 207.86 cm^{-1} , and 493.74 cm^{-1} (Perez-Osorio et al., 2018). In previous studies, these vibrations indicate the degree of rotation and torsion in the MA and cause disorder of the arrangement of perovskite structure and changes in the Rashba spin-orbit coupling (bin Mohd Yusoff et al., 2021). It has been known previously that of the many hybrid organic-inorganic perovskites have a changed structure, basically this change is caused by the effect of the movement of organic molecules between the octahedral so that the observed phase changes or can be called the dynamic phase (Jaffe et al., 2016). In the high frequency area, we observed that the MA experienced rocking and stretching vibration modes around 642.53 cm^{-1} and 709.02 cm^{-1} . Both of these vibrations are very sensitive to hydrogen which allows attractive forces on the bond (Cabana & Sandorfy, 1962).

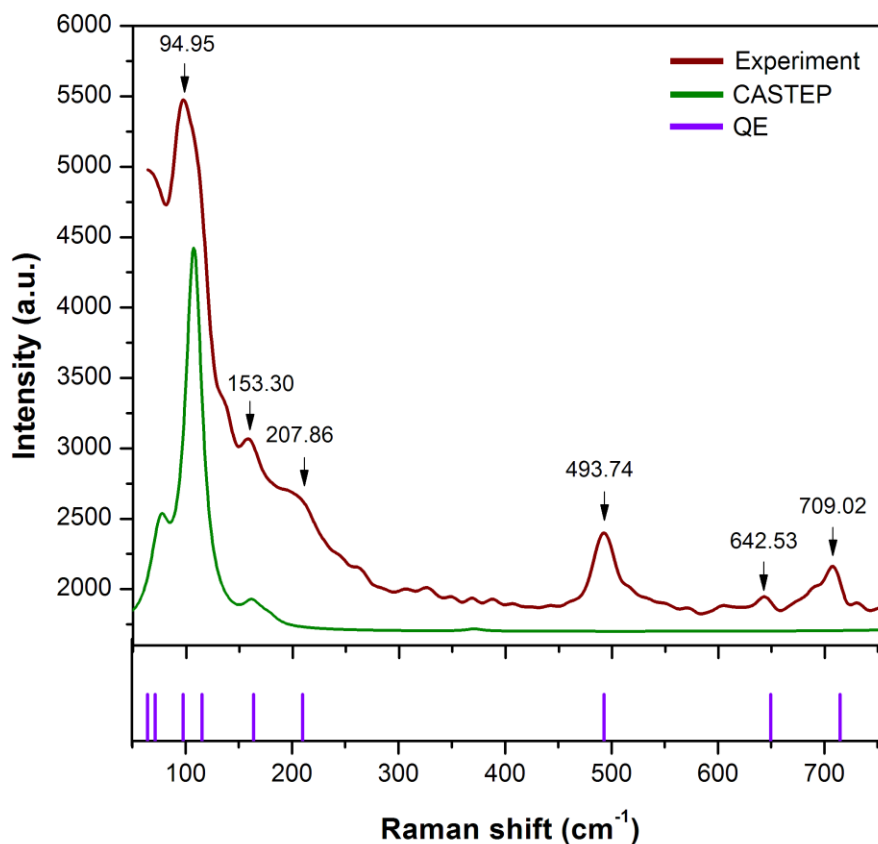


Figure 23. A Comparison between observed and calculated Raman spectra of MAPbI_3 in the low-frequency range up to 760 cm^{-1} . The vertical arrows are guides to the eye and indicate the frequencies of the Raman modes with the highest intensity. The green lines and purple sticks have been obtained from the first-principles calculation through CASTEP codes and QE codes, respectively.

We use first-principles utilizing the CASTEP and QE algorithms, which are depicted in Figure 22, to support the outcomes of the prior experiment. This section fully relaxes the orthorhombic structure with the Pnma space group while still taking into earlier research (Pérez-Osorio et al., 2015). We discovered at least four Raman

modes in the Pbl3 framework and % Raman modes in organic MA in the 60 cm^{-1} to 760 cm^{-1} frequency range based on QE predictions. These predictions, particularly the estimated vibrational modes of organic MA, appear to be consistent with observation. However for CASTEP calculation, it seems under estimate, it might be due to the differences set up of energy cut-off from QE calculation. Additional investigations reveal that the expected modes shift manifests at 64.31 cm^{-1} , 71.31 cm^{-1} , 97.65 cm^{-1} , and 115.27 cm^{-1} , which are primarily corresponded to Pb-I bending and stretching modes. The observed peak distribution differs from spectral observation, which may be the result of the seen peaks merging in the same frequency band.

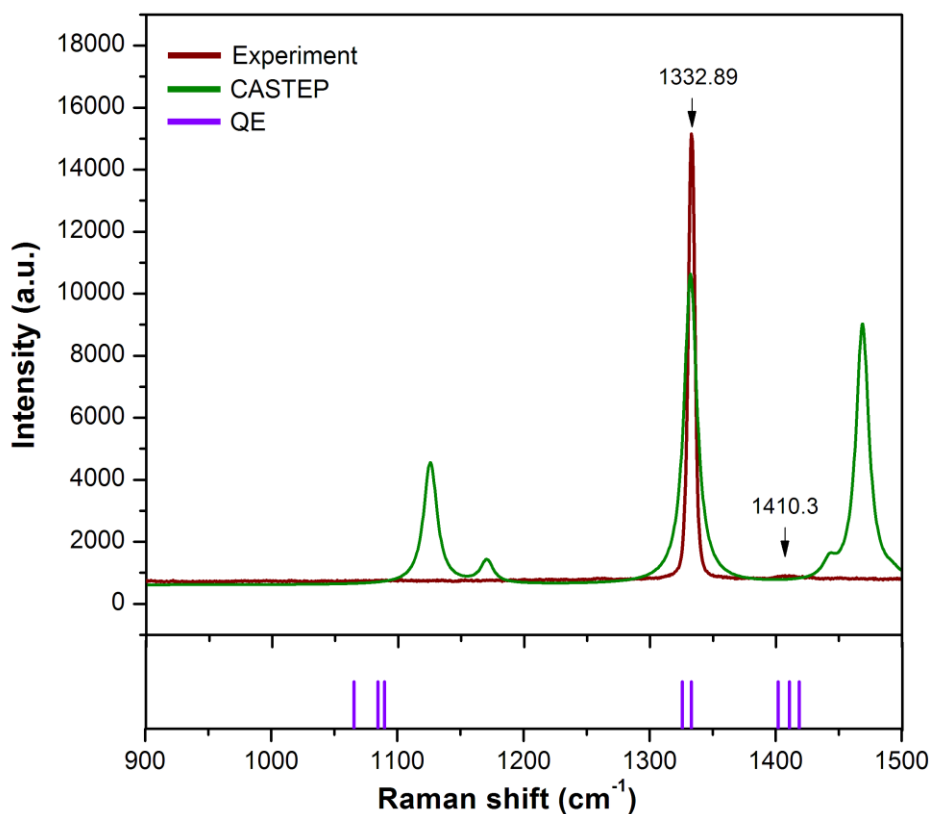


Figure 24. The Raman spectra of MAPbI₃ observed at fingerprint frequency range, while their predictions from CASTEP and QE codes are included for comparison. For clarity, the Raman spectra are measured at ambient pressure and room temperature.

We also further describe the Raman spectra at fingerprint frequencies from 900 cm⁻¹ to the highest at 1500 cm⁻¹, as shown in Figure 23. The fingerprint frequency is usually populated by Raman modes associated with hydrogen bond vibrations. The highest intensity around 1332.89 cm⁻¹ and small feature at 1410.3 cm⁻¹ corresponds to C–H bending and N–H bending with E-symmetry (Pérez-Osorio et al., 2015). However, the observations of Raman modes are quite dissimilar from predicted results. However, the observations of Raman modes are quite dissimilar from the predicted results. The observed spectra around 1100 cm⁻¹ cannot be observed due to highly sensitive to structural distortions of the PbI₆ octahedral framework. Therefore, we also suspect that in this frequency area hydrogen bonds do not have any interactions with other atoms.

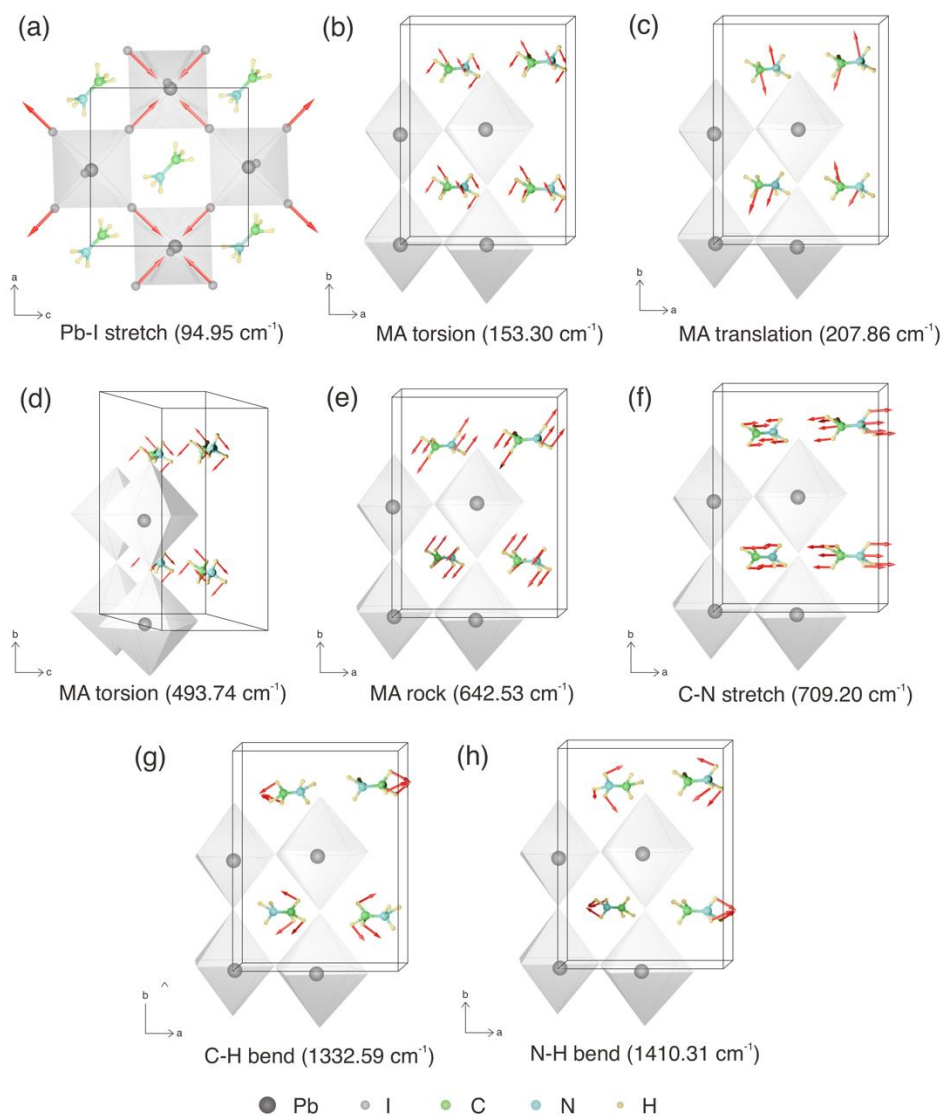
The computational approach proves that there are 8 internal vibrations of organic MA and indicated as CH₃–NH₃ rocking, C–N stretching, and H–bonds bending modes. The majority of the MAPbI₃ vibration modes are Raman active with varying relative intensities because organic MA is non-centrosymmetric. According to the analysis of each factor group, it is possible to anticipate that the vibrational modes of

hydrogen bonding with an organic MA preponderance will arise at 1370, 1403, 1419, 1533, and 1544 cm^{-1} (Haase, 1972). This older study is consistent with the findings of our investigation using QE codes, however in the CASTEP forecast, the peak positions clearly shift to a higher frequency.

No. Mode	Sym- metry	Calculated Raman Shift(cm^{-1})	Observed Raman Shift(cm^{-1})	Character
1	B_{3g}	64.31		Pb-I-Pb bend
2	A_g	71.31		Pb-I-Pb bend
3	B_{1g}	97.65	94.95	Pb-I stretch (sym.)
4	B_{2g}	115.27		Pb-I stretch (asym.)
5	B_{1g}	163.98	153.30	MA torsion
6		209.83	207.86	Translation/liberation
7	A_2	493	493.74	MA torsion
8	E	649.64	642.53	MA rock
9	A_1	709.77	709.20	C-N stretch
10	E	1065.62		MA rock
11	A_1	1084.54		C-N stretch
12	E	1089.69		MA rock
13	A_1	1325.83		C-H bend (sym.)
14	E	1333.14	1332.59	C-H bend (asym.)
15	A_1	1402.01		N-H bend (sym.)
16	E	1411.14	1410.31	N-H bend (asym.)
17	E	1418.68		N-H bend (asym.)

Table 1. Symmetry, calculated Raman, and observed Raman as well as vibrational characters.

The comprehensive analysis of the observed Raman shifts and the confirmation of the DFT calculation can be found in table 1. $A_g + 2B_{1g} + B_{2g} + B_{3g} + A_2 + 4A_1 + 6E$, where g type represents inversion symmetry and E denotes double degeneration, are the estimated normal modes at a specific point. The projected Raman shift, which is in good agreement (within 0.5-1%) with actual Raman peaks, produces nearly all of the Raman peaks. A single PbI_3 network peak is observed at $94.95 \text{ (cm}^{-1}\text{)}$, which is described as symmetric Pb-I stretching, as was previously mentioned. The large and varied strength of the B_{1g} symmetric vibrational modes in this case. Therefore, it is impossible to identify between asymmetric Pb-I stretching and Pb-I-Pb bending. The vibrational modes of organic MA are very hard to identify, especially at modes 10, 11, and 12. It is safe to assume that the current peak organic MA observation captures all of the $MAPbI_3$ crystal's vibrations.



CHULALONGKORN UNIVERSITY

Figure 25. Schematic representations of Raman vibrational modes in MAPbI_3 . The vibrational modes of PbI_3 framework from top view where Pb atoms in black color and I atoms in grey color (a); and the internal vibrational modes of organic MA from side view where C, N, and H are in green, blue, and yellow color, respectively (b-h).

The red arrows are the vibrational movements.

The schematic representations of each of the MAPbI₃ vibrational modes that have been observed are shown in Figure 24. The organic MA atomic movements with the highest Raman intensity are depicted in the schematic. Organic MA's vibrational mobility is probably caused by their remarkable sensitivity to the microenvironment (Xie et al., 2016). Overall, we listed the evidence for the MAPbI₃ active modes, from low to high frequency: Pb-I stretching modes of B_{1g} symmetry are located at 94.95 cm⁻¹, MA torsion modes of B_{1g} symmetry are located at 153.30 cm⁻¹, translation/libration modes of organic MA are located at 207.86 cm⁻¹, MA torsion modes of A₂ symmetry are located at 493.74 cm⁻¹, MA rocking modes of E symmetry are located at 642.53 cm⁻¹, C-N stretching modes of A₁ symmetry are located at 709.20 cm⁻¹. In a separate report, we went through how its vibrational modes changed as the hydrostatic pressure increased.

4.2. Lead-Free Double Perovskites

The synthesis method of Cs₂TiBr₆ using a vapor solution reaction has been used in previous studies. In this work, we focus on using a solution synthesis method because it is easier and cheaper. The use of dilute HBr acid as much as 20 mol% is known to reduce the incomplete reaction due to the high volatility of the reaction. The ratio of the molar ratio between CsBr and TiBr₄ is 1:0.7 where the Ti content must be increased in relation to the stoichiometry. A small molar ratio like 1:0.5 cannot synthesize Cs₂TiBr₆ powder because TiBr₄ reacts quickly with air in acidic HBr,

so TiBr_4 does not react more fully with CsBr (He et al., 2022). Therefore, the use of TiBr_4 is recommended not to get pure powder. Then, further heating was carried out to increase the crystallization level of the powder and to maintain the resistance of TiBr_4 at room temperature. Previous studies have compared various treatments of heating temperature and it affects the decomposition of powders.

Figure 21 shows a photograph of the solution after stirring, the unheated wet powder and the annealed dried powder which has a red dark color as reported in the previous work. To ensure the purity and determine the structure of the double perovskite powder, we have employed XRD as shown in Figure 25. A diffractometer (Bruker D8 ADVANCE) with $\text{Cu K}\alpha_1$ X-ray source operating at 40 kV/30 mA was used to conduct XRD observations. XRD spectra show dominant peaks around 29° , 33° , 47° , and 57° which identify the Cs_2TiBr_6 crystal plane of (222), (400), (440), and (622), respectively. This shows the consistency with the previous works with both the vapor deposition method and the solution method (Euvrard et al., 2020). However, there are some visible small peaks and peak splitting which are seen suggesting additional phase with different lattice constants. From the diffraction pattern, it can be calculated by using Bragg's law that the value of the lattice constant of Cs_2TiBr_6 is around 10.87 \AA . From the analysis obtained, we conclude that the crystalline phase in Cs_2TiBr_6 is cubic $\text{Fm}\bar{3}\text{m}$ at room temperature. Furthermore, the highest intensity in the crystal plane 222 indicates the presence of a TiBr_6 octahedron in the cubic

structure. However, the powder turned into a liquid after being used in the XRD experiment because Cs_2TiBr_6 was easily contaminated and decomposed on exposure to water. Previous findings have shown changes in the XRD spectrum of Cs_2TiBr_6 under oxygen, moisture, thermal and light conditions (Chen et al., 2018).

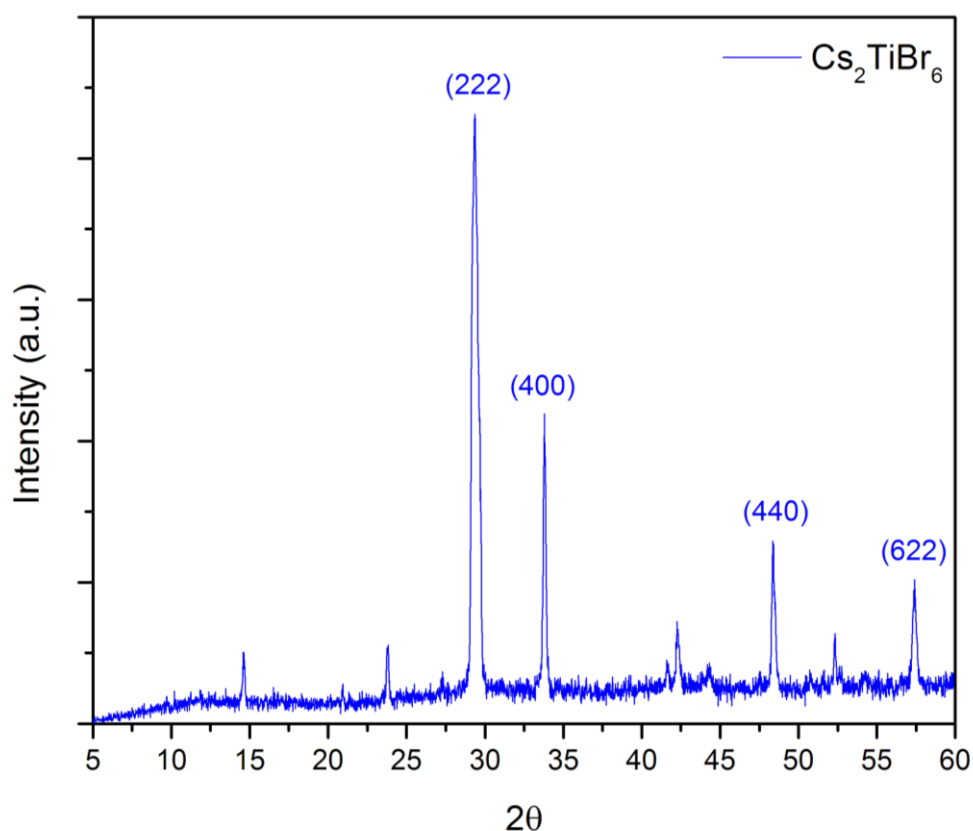


Figure 26. XRD spectra of the double perovskite Cs_2TiBr_6 powder gained by solution synthesis method.

We have also analyzed the vibrational properties of Cs_2TiBr_6 at room temperature using Raman spectroscopy. The Raman spectrum of Cs_2TiBr_6 was measured in the frequency range 50 cm^{-1} to 750 cm^{-1} as depicted in figure 26. Since

only partial Raman spectra of Cs_2TiBr_6 have been reported, we provide a more detailed analysis of the experimental Raman spectrum. In addition to the requirement for accurate assignment of Raman active phonons, this technique is useful in distinguishing intrinsic from inclusion Raman features. In this observation, there are five major peaks that appear at frequencies around 52.4 cm^{-1} , 120.4 cm^{-1} , 198.8 cm^{-1} , 250.7 cm^{-1} , and 500.1 cm^{-1} , corresponding to \mathbf{u}_1 , \mathbf{u}_2 , \mathbf{u}_3 , \mathbf{u}_4 and \mathbf{u}_6 vibrational modes, respectively, observed under ambient conditions. As previous report, vibrational mode of \mathbf{u}_1 and \mathbf{u}_2 belong to Cs-Br interaction and represented as E_g and A_{1g} Raman active mode. Meanwhile, vibrational modes of \mathbf{u}_3 , \mathbf{u}_4 , and \mathbf{u}_6 were identified as interactions of octahedral TiBr_4 , this was agreed with previous work. It is known that solvent and excitation wavelength do not affect the high intensity at \mathbf{u}_3 . We tentatively observed the three vibrational modes are identified as stretching TiBr_6 octahedral. In general, the vibrational properties of TiBr_6 greatly affect the stability of the cubic structure.

In addition, a CASTEP code-based calculation is used to find the expected Raman intensity. From the previous XRD experiment we got the parameters to model the structure of Cs_2TiBr_6 where with the space group $Fm\bar{3}m$ and the lattice constant of 10.87 \AA at ambient conditions. We have optimized the geometric structure of the unit cell before calculating. By implementing an ultra-soft pseudopotential with an Monkhorst-Packs scheme energy cut-off of 80 Ry and a K-point of $4 \times 4 \times 4$, we

calculate the phonon properties. Figure 26 shows the Raman spectrum of the calculation results which are almost similar to the observed results. However, we could only find 3 Raman peaks including 1 active Raman of Cs-Br and 2 active Raman of TiBr_6 at frequencies around 108 cm^{-1} , 182 cm^{-1} , and 241 cm^{-1} , respectively. We remark that Brivio et al. similarly reported an overestimation of the Raman peak's strength by computations (Brivio et al., 2014). We also found that our calculations significantly under estimate the Raman intensity of the same peak. Therefore, it seems that we consistently under estimate the Raman of both Cs-Br and TiBr_6 modes. It is probable that SOC in Titanium and anharmonicity have an impact on these modes Raman intensities. However, it has been demonstrated in the past that SOC effects only slightly alter the IR intensities (Perez-Osorio et al., 2017). Despite the shift to different frequency values, this result is still in line with the experiment, especially at high intensity at 182 cm^{-1} which is owned by TiBr_6 as strong stretching mode.

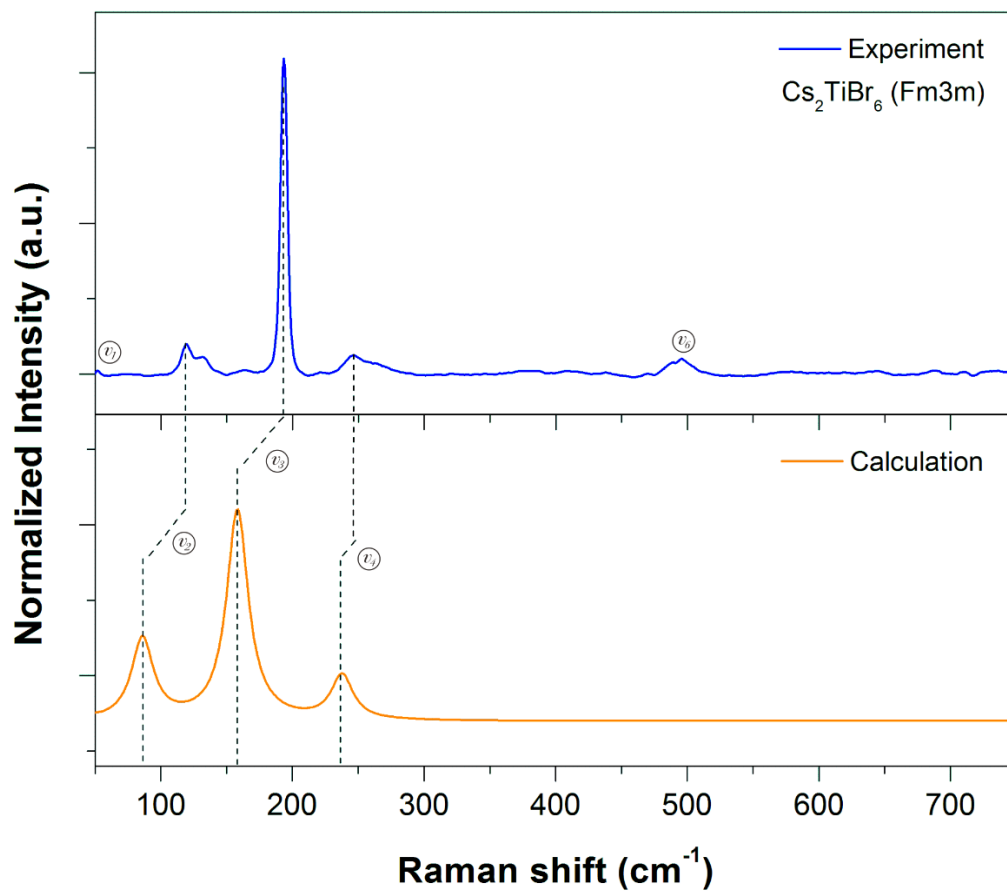


Figure 27. A comparison between observed Raman spectrum of Cs_2TiBr_6 cubic phase

$Fm\bar{3}m$ with the calculated Raman spectrum by using CASTEP code.

CHULALONGKORN UNIVERSITY

4.3. Phase Transition under Pressure

4.3.1. Hybrid organic inorganic perovskite phase transition

In this section, we discuss the hybrid perovskite MAPbI_3 where related to high pressure-induced vibrational evolution. By combining Raman spectroscopy with DACs, a thorough study of the phase change and the interaction of its organic-inorganic molecule under hydrostatic pressure was conducted. As shown in Figure 27, under

six steps of applied pressure, the spectra in the low-frequency band between 60 and 760 cm^{-1} exhibit a variety of peak position distributions. The PbI_3 octahedral framework stretch is seen at ambient pressure (0 GPa) in the first peak about 94 cm^{-1} , which also has the highest and most intense intensity when compared to other peaks. This shows clearly that PbI_3 framework vibrations produce more significant dynamical disorder in the structural phase at 0 GPa. Additionally, a wide range of the Raman peak of MA liberation is seen, spanning 150 cm^{-1} to 270 cm^{-1} . This suggests that the MA is easily diverted in the PbI_3 octahedral framework at ambient pressure.

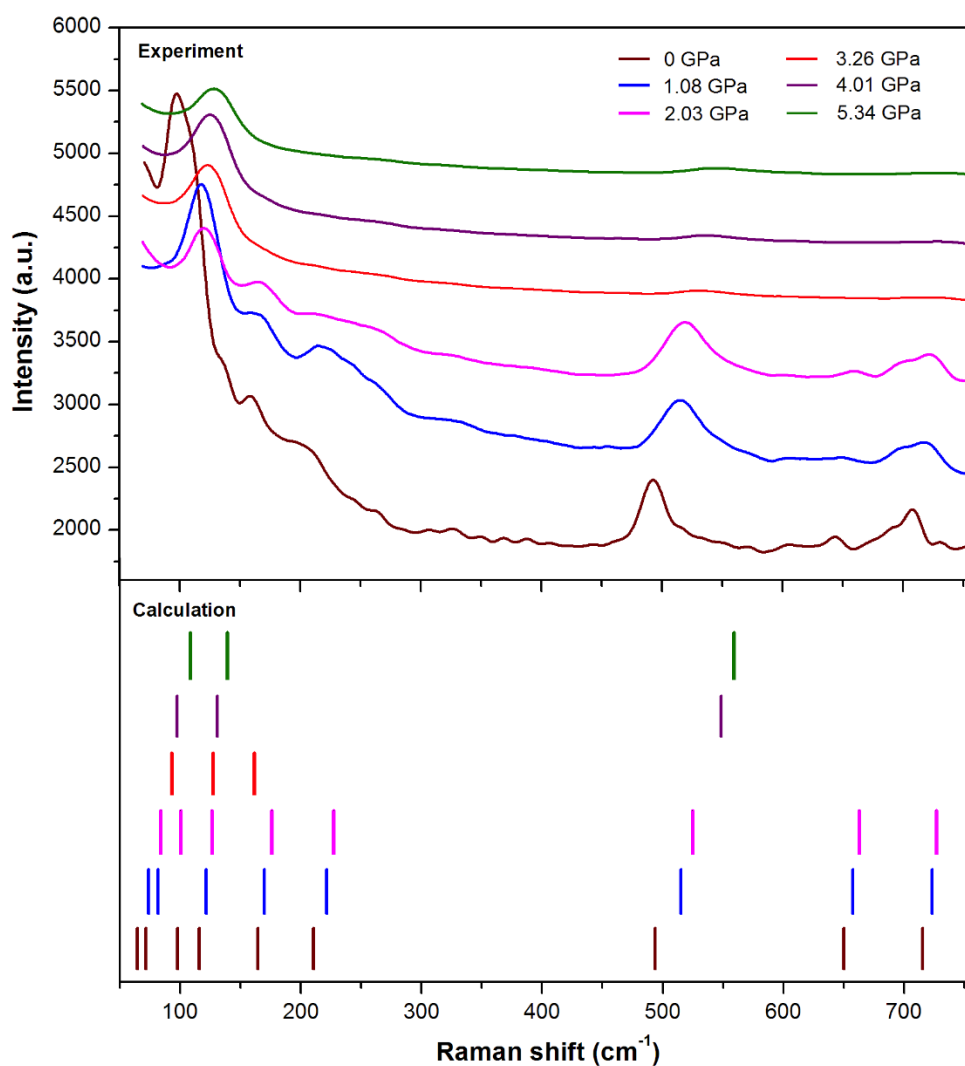


Figure 28. Observed Raman spectra from MAPbI₃ upon compression (upper chart) and comparative results of Raman modes by DFT calculation (lower chart).

Each peak's strength gradually decreases as pressure rises up to 2.03 GPa, especially the peaks of Pb-I and organic MA that are located below 300 cm⁻¹ in height. Although the MA torsional and stretching modes continue to vibrate under this pressure state, it can be attributed to the restraint of Pb-I stretching and translation modes under compression. At this pressure, however, the vibration of MA rocking at a radius of 645 cm⁻¹ was hardly audible. In the presence of pressure, there is theoretically a modest likelihood of vibrational interaction between PbI₃ frameworks and organic MA. As a result, the organic MA has a propensity to travel freely in the spaces between inorganic cages.

Beyond 3.26 GPa, a drastic change in the spectra occurs, with the majority of the organic MA peaks disappearing and only the peak of the Pb-I stretching mode remaining. It was suggested that shortening PbI₃ frameworks under high pressure was demonstrated by the vibrational movements of organic MA after freezing. The other explanation is because their closely packed structure causes organic MA to become trapped in PbI₃ frameworks in arbitrary locations, which breaks the Pb-I-Pb bending vibrational modes as evidenced by the disappearance of modes at 100 cm⁻¹. Even though it is not as obvious, the torsional movement of organic MA reappears at high pressures of 4.01 and 5.34 GPa. Jaffe, A. et al. and Marek, S. et al. recently noticed

the outcome in the shortening of Pb-I bonds and an increase in the angle of Pb-I-Pb as well as how this causes crystal amorphization (Jaffe et al., 2016; Szafranski & Katrusiak, 2016). However, we thought that even at pressures as high as 5.34 GPa, Pb-I stretching modes would continue to vibrate.

As seen in the lower chart of Figure 27, we also used the DFT approach to predict the likelihood of the modes as a comparison. We predict additional PbI_3 vibrational modes at a related frequency that could have an effect on the peak intensity. Additionally, it is possible to clearly distinguish the internal vibrations of organic MA, which provide typical motions and occupy PbI_3 frameworks. These internal vibrations include torsion (153.30 and 493.74 cm^{-1}), translation (207.86 cm^{-1}), rocking (642.53 cm^{-1}), and stretching modes (709.20 cm^{-1}). The MAPbI_3 dynamical disorder. Under a pressure of 2.03 GPa, all of the modes are still active. After this pressure, a new phase with some modes disappearing at frequencies around 230 cm^{-1} , 550 cm^{-1} , 660 cm^{-1} , and 740 cm^{-1} is projected as a comparable Raman mode consequence at 3.26 GPa. We can still forecast a new mode at about 550 cm^{-1} even though we were unable to clearly observe a new peak beyond 4.01 GPa.

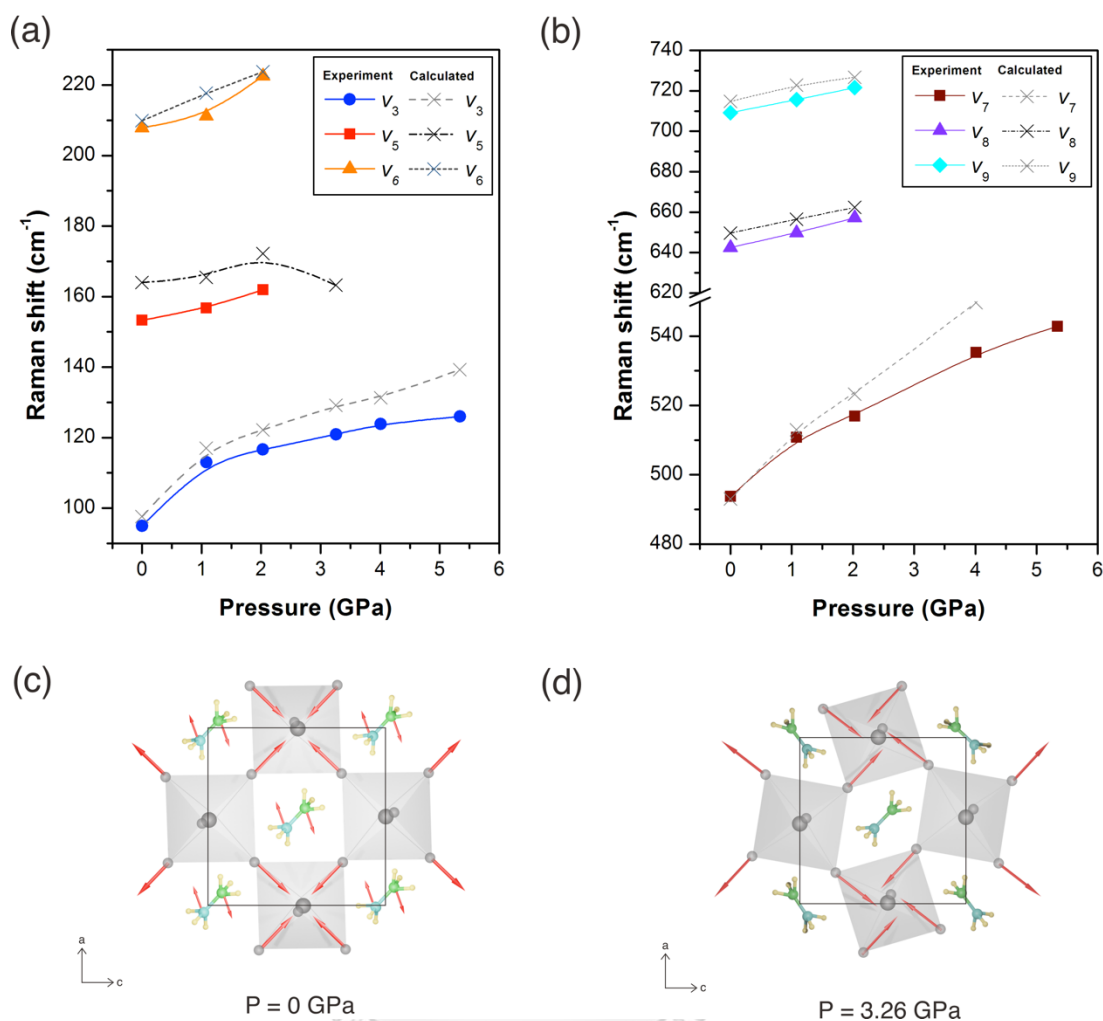


Figure 29. The evolution of Raman shift of MAPbI₃ as a function of pressure across frequency range 50–225 cm⁻¹ (a), 480–740 cm⁻¹ (b), the schematics of MAPbI₃ perovskite illustrate the vibrational motions including Pbl₃ framework stretching modes and internal MA modes under ambient condition (c) and hydrostatic pressure at 3.26 GPa (d).

Figures 28a and 28b show considerable shifts over phase transitions under hydrostatic pressure, which is another fascinating debate on the observation of

vibrational spectra in MAPbI₃. The maxima of each vibrational mode, such as the Pb-I stretching mode as ν_3 , MA torsional mode as ν_5 and ν_7 , translation mode as ν_6 , MA rocking mode as ν_8 , and C-N stretching mode as ν_9 , shift to a higher frequency with increasing pressure. The frequency of ν_3 and ν_7 rose more than the other modes among these vibrational modes at 1.08 GPa. Additionally, at pressures greater than 3.26 GPa, ν_5 , ν_6 , ν_8 , and ν_9 disappear.

In terms of the patterns, we noticed at least three phases with pressures ranging from 0.0 to 5.34 GPa. In particular, the freely moving organic MA (i.e., torsion, translation, rocking, stretching, and bending) and the vibrations of PbI₃ frameworks as shown in Figure 28c, were expected to cause structural variation under zero pressure. Similar results were obtained when pressure-induced structural evolution of MAPbI₃ was recently discovered by XRD; their structure phase was identified as cubic Pm3m at room temperature, with a high level of positional disorder of organic MA (Baikie et al., 2013). Since the spectrum data cannot show the symmetry of the crystal phase in this instance, we can only conclude that the first phase of MAPbI₃ is the dynamic phase. Then, a significant shifting of ν_3 and ν_7 will indicate the second phase at 1.08 GPa. It was reinforced by earlier evidence, which showed that the frequency ranges of 70 cm⁻¹ and 510 cm⁻¹ are where the intensity of ν_3 and ν_7 dramatically collapses. The behavior of the second phase is consistent with the PbI₃ framework-distorted cubic phase with Im3 (Matsuishi et al., 2004; Szafranski &

Katrusiak, 2016; Wang et al., 2015). Additionally, the vibrational characteristics of organic MA are unaffected by the cubic phase distortion caused by pressure. According to decreasing the unit cell volume in compression, Figure 28d shows that the organic MA's vibrational motions are stopped. The organic MA vibrational modes can be compressed in this phase at 3.26 GPa, and the disappearance peaks (ν_5 and ν_6) suggest that the organic MA is not moving in the voids of the inorganic cage. The saturation intensity around the frequency at which the vibration of organic MA is taking place is related to the new phase as a static phase. It is thought that the structural evolution begins with a highly disordered phase and transitions into an orthorhombic phase at relatively high pressure and temperature (Onoda-Yamamuro et al., 1990; Ou et al., 2016). Beyond 4 GPa, the structure undergoes a complete amorphous transformation along with an increase in MA torsional modes.

As seen in Figure 29, under elevated pressure, DACs showed detail in the spectrum in the finger print region. The well-defined peak at around 1300 and 1400 cm^{-1} at ambient conditions has been assigned to the bending modes of the C-H and N-H vibrations, respectively. Due to the larger bond enthalpy of C-H, the measured spectrum intensity of C-H bending is significantly stronger than the N-H bending, and the peaks splinting is astonishingly obvious between them. It is well known that the Pb16 octahedra influence molecular hydrogen bonding and motion by increasing the

tilt of the octahedra, which increases the interatomic force between hydrogen atoms and iodide ions and increases the degree of H-bonding (Xie et al., 2016).

after compression, The intensity of the C-H peaks remains high despite the change to higher energy. As more pressure indicates a smaller unit volume and lessens C-H bending, the peak of C-H shifts significantly. When the pressure reaches 3.26 GPa, the structure enters the static phase, which is indicated by the presence of peaks of N-H bending modes, which show that the H movement does not interact with the PbI_3 framework. As a result, the N-H bending mode peaks lose their intensity as pressure increases up to 3.26 GPa. It may be connected to a recent finding that tilt disordering PbI_3 frameworks are made possible by the same H-I and N-H bonding distances (Jaffe et al., 2016; Park et al., 2017). By tilting the PbI_3 , even the body stiff of organic MA may be easily accommodated in the anisotropic cubo-octahedra (Swainson et al., 2007).

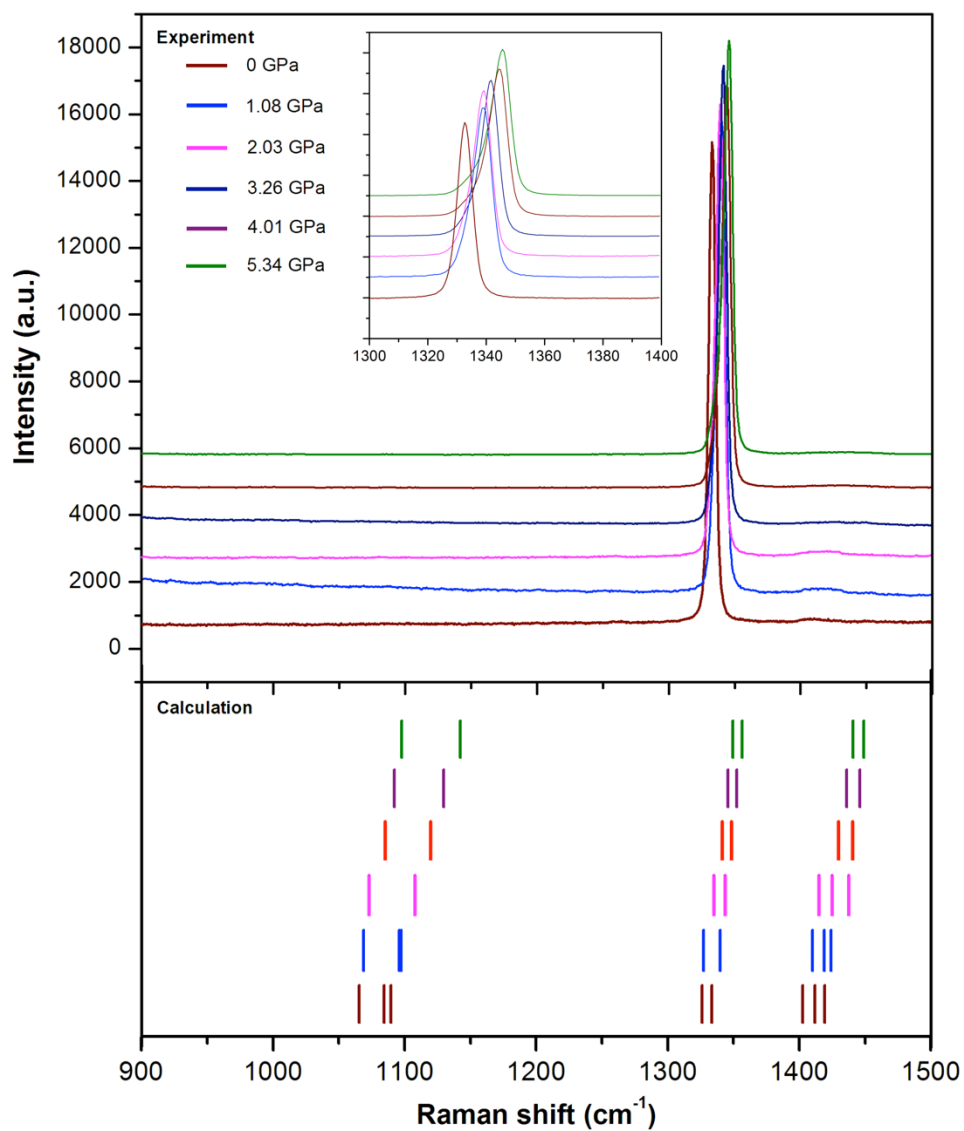


Figure 30. The pressure-induced Raman spectra evolution of MAPbI_3 across fingerprint range where observed data shows on an upper chart and calculated data shows on a lower chart. Inset: Raman shift dication.

4.3.2. Double perovskite phase transition

We also carried out the high-pressure Raman experiments to track the structural transformation under pressure of Cs_2TiBr_6 . The evolution of Raman spectra

in the range of 50 to 750 cm^{-1} is shown in figure 30. As previous discussion, in the initial phase, namely α -phase observes under ambient conditions, there are five strong peaks at 52.4 cm^{-1} , 120.4 cm^{-1} , 198.8 cm^{-1} , 250.7 cm^{-1} , and 500.1 cm^{-1} , corresponding to ν_1 , ν_2 , ν_3 , ν_4 and ν_6 vibrational modes, respectively (Kamisuki & Maeda, 1973; Nguyen et al., 2020). These modes were assigned for the vibrational modes of the TiBr_6 octahedron except the ν_1 and ν_2 which are the vibration of Cs^+ . When the pressure is increased to 7.4 GPa, the Raman spectrum still looks the same which indicates that there is no interaction change so that the phase still looks similar to the initial shape. However, only the energy is shifted to a higher level, this indicates the occurrence of compression in the structure inside. After being given further pressure, the vibrational ν_6 was observed to decrease in the intensity which eventually disappeared. The intensity reduction is due to change of octahedral network structure. Meanwhile, around the frequencies of 408.3 cm^{-1} and 613.7 cm^{-1} , new peaks appeared with low intensity corresponding to ν_5 and ν_7 . This vibration mode may appear instead of ν_6 , this proves that the stretching mode on the octahedral TiBr_6 disappears and changes the orientation of the vibrations when a pressure is applied up to 10.4 GPa. Therefore, we believe that at pressures of about 8.8-10.4 GPa, the double perovskite phase begins to transition from α -phase to β -phase. Raman spectra changed drastically above 11.9 GPa, the peaks appeared as indicated with star, which are ν_4 , ν_5 , and ν_7 around the frequency of 351.2 cm^{-1} ,

450.1 cm^{-1} , 673.5 cm^{-1} , respectively. Similar to those reported for pure TiBr_6 , it appears that the new peaks are vibrational modes of octahedral TiBr_6 , all of which are torsional modes (Kamisuki & Maeda, 1973). At this pressure, the octahedral TiBr_6 interaction was shown to increase. Previous work also explains the existence of a contraction causing J-T distortion is fully suppressed due to octahedral tilting. This causes a significant phase change which becomes a complete second phase or β -phase. Until finally at a high pressure of about 20.6 GPa, the phase change is not so visible anymore. Previous work had also predicted a third phase that should occur at 30 GPa. We also observed a change in the Raman spectrum during decompression seen in the yellow line spectra. On decompression, all peaks return to their initial form and shift to low energy. We suggest that these changes are reversible and all three TiBr_6 torsions disappear upon decompression.

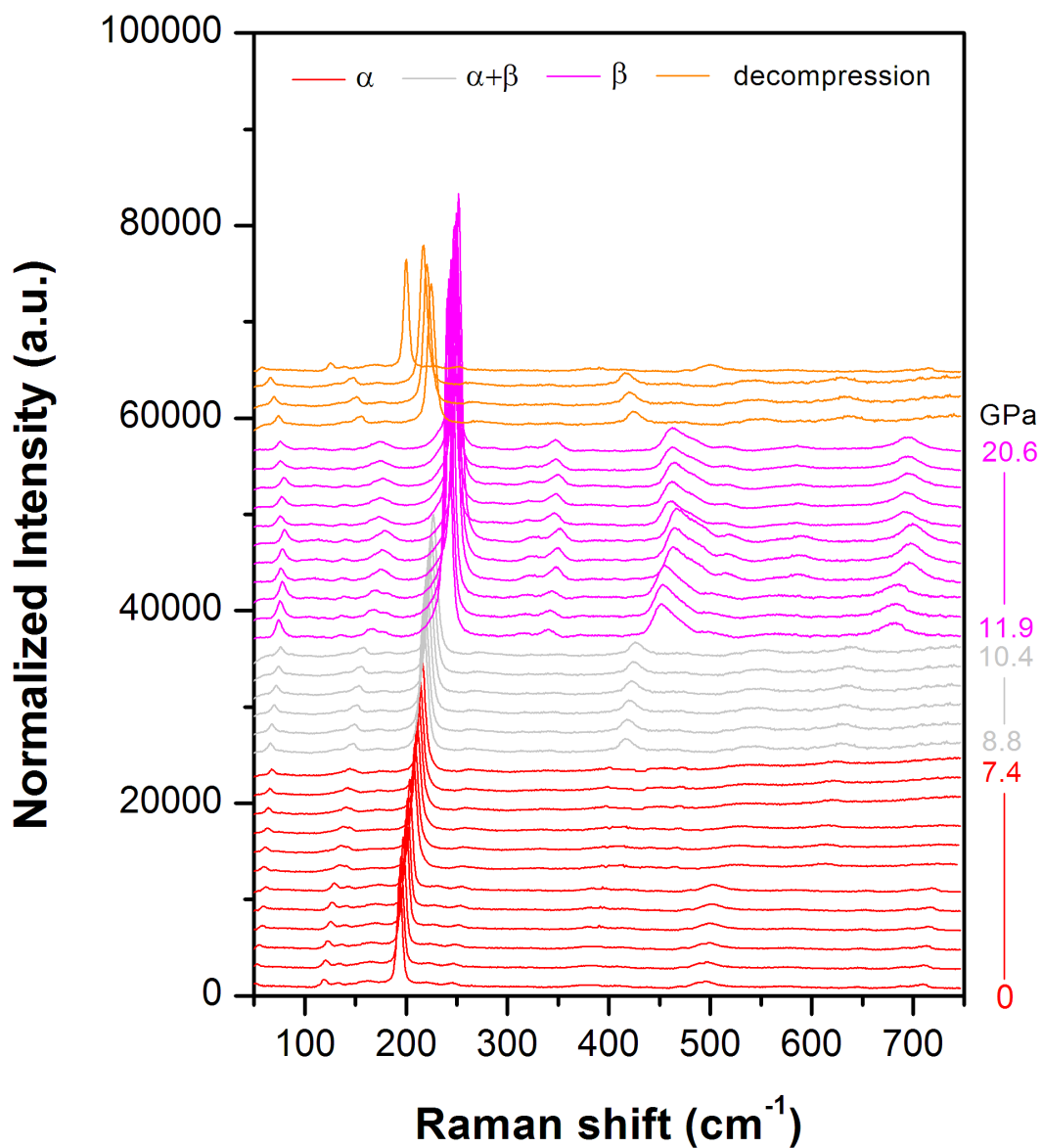


Figure 31. Raman patterns of double perovskite Cs_2TiBr_6 upon compression up to 20.6 GPa and decompression to ambient pressure.

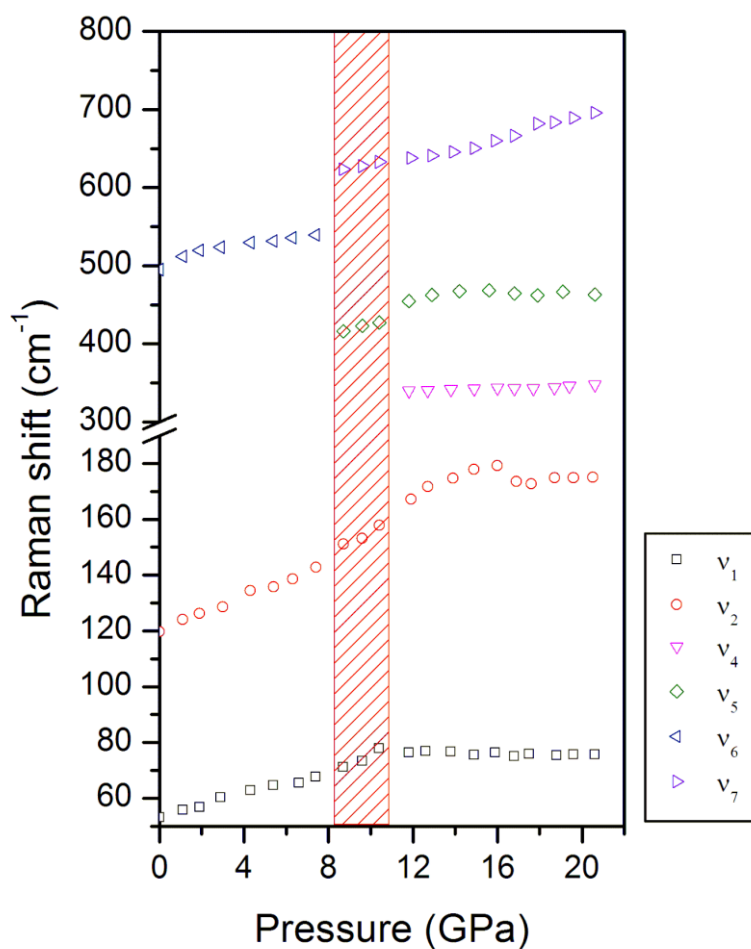


Figure 32. The Raman shift evolution of double perovskite Cs_2TiBr_6 as a function of pressure across frequency range $50\text{--}800\text{ cm}^{-1}$

Our calculations are also nicely reproduce frequency-depended Raman intensity of almost some of the peaks observed in the experiments. the dashed black lines in figure 32 represent our suggested attribution of the Raman spectra. Overall, theory and experiment are in the good agreement where in the second phase shows the peak of the Torsional Mode of Cs_2TiBr_6 including ν_5 and ν_7 . However, some vibration modes such as ν_1 , ν_2 , and ν_4 are not visible in the

calculation and our calculation appear to under estimate the energy of the measured peaks in the case of the torque of modes of the cations by as much as 50 cm^{-1} . It is still unknown where this difference came from. An explanation might be that the Raman intensities of these modes are influenced by VdW interactions, SOC, and anharmonicity (as opposed to their frequencies). Prior Research has demonstrated that Soc and VDW impacts the Frequencies closer to Experiment.

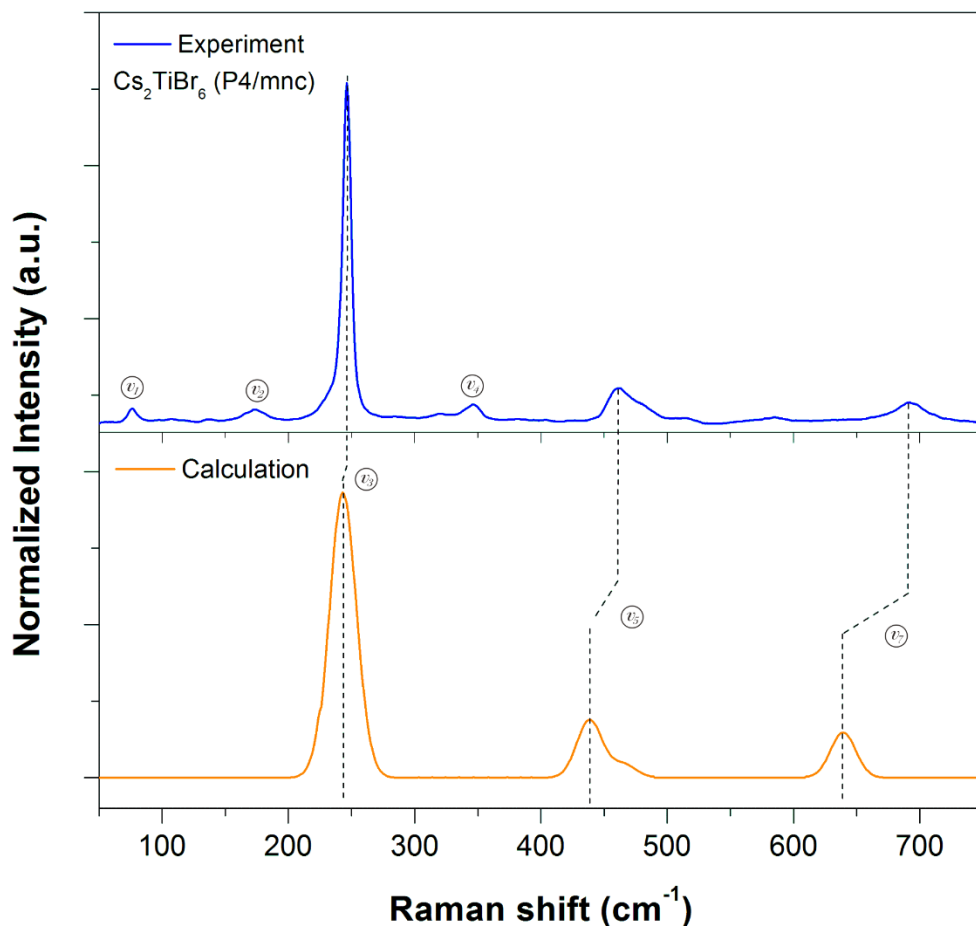


Figure 33. A comparison between observed Raman spectrum of Cs_2TiBr_6 tetragonal phase $P4/mnc$ with the calculated Raman spectrum by using CASTEP code.

As illustrated in Fig. 33, the variation of pressure with total enthalpy is used to evaluate the values of the phase transition pressures. We get the total enthalpy from the BEM-OS calculations as in the previous work. Fig. 33b and 33c shows the difference in the structure and together the view from Y axis. Under pressure, the compound Cs_2TiBr_6 undergoes two phase changes. The first phase is identified when the ambient pressure approaches below 11 GPa, it is clear that the total enthalpy of the $\text{Fm}\bar{3}\text{m}$ cubic phase is lower than P4/mnc . The cubic structure is having good arrangement and engaged JT distortion when pressure is applied. It also allows it to have a stretching vibration mode rather than bending or torsion mode. Then, the second phase occurs after 11 GPa, where the total enthalpy tetragonal phase P4/mnc cross under $\text{Fm}\bar{3}\text{m}$. The tetragonal phase stabilizes at this pressure and the octahedral tilting acts to replace JT distortion. The existence of octahedral tilting leads to new appearance of torsion modes. All this is reinforced by the obtained Raman results.

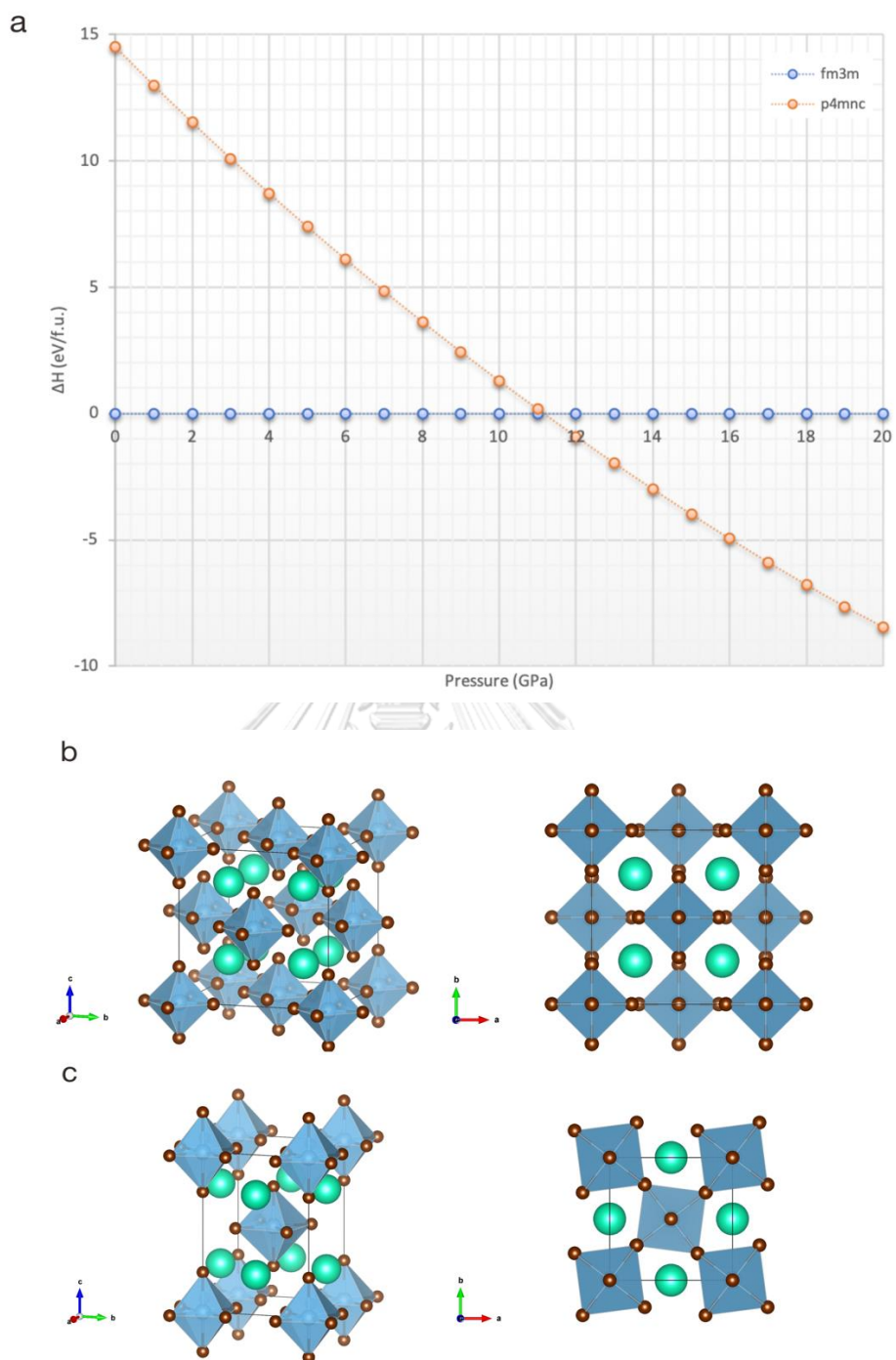


Figure 34. Total enthalpy as function of pressure (a), cubic phase $Fm\bar{3}m$ (b), and tetragonal phase $P4/mnc$ (c).

The structural stability of a material can be determined by analyzing its lattice dynamical properties. Previously, the lattice dynamical properties of cubic $Fm\bar{3}m$ have been reported by Diwen Liu (Liu et al., 2021). However, they only show the properties of the cubic phase even if the pressure is extended to 15 GPa. For comparison, we also predicted the phonon dispersion spectra of in their stable phases in the tetragonal phase $P4/mnc$. The obtained results are shown in Fig. 34, together with the total and partial densities of states. As we clearly seen, no imaginary at any wave vector is found in the tetragonal structure. So, the structures are dynamically stable at ~ 11 GPa. We also expect this stability to be maintained even though the applied pressure reaches 20 GPa. In addition, the phonon frequencies for the optical branches of tetragonal phase less than the cubic ones.

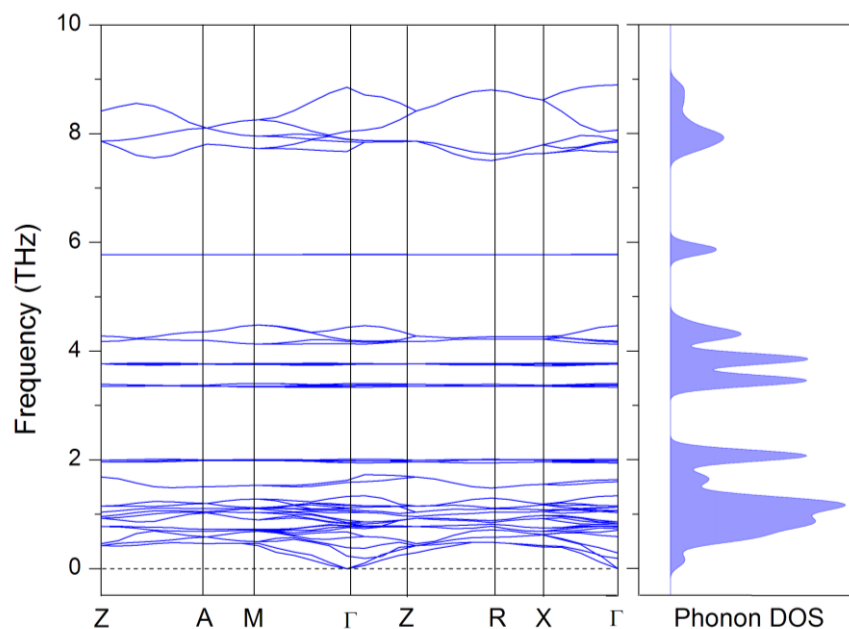


Figure 35. Calculated phonon dispersions and phonon density of states for Cs_2TiBr_6

in tetragonal phase $P4/mnc$.

4.4. Optical Properties under Pressure

Piezochromic luminescent materials have been thoroughly investigated for their potential use in optical data storage, pressure sensors, led and optoelectronic devices (Lv et al., 2019). These materials exhibit remarkable emission discoloration in response to external mechanical stimuli (such as grinding, pressing, and stretching). Perovskite material is one that has the ability to piezochromism (Jiang et al., 2021). However, previous work has only focused on the effect of pressure on the energy gap. Using spectral measurements and external pressure via the diamond anvil cell (DAC) technique is an efficient way to conduct in situ research on optical qualities including photoluminescence (PL) emission. Therefore, in this discussion, we will present the results of the pressure-induced photoluminescence of both hybrid and double perovskite materials. We also explain the relationship between phase changes and changes in optical properties under pressure.

It has previously been proposed that the nature of the octahedra may have a significant impact on perovskite emission (Ma et al., 2018). As a result of structural modification with variable pressure, Altered PL properties may be expected. We track the PL emission of double perovskite Cs_2TiBr_6 as variation of pressure as seen in figure 35. The pressure-dependent PL spectra for our sample were collected up to 20.6 GPa and PL spectra were recorded at the excitation emission wavelengths of 600 to 900 nm. We observe a slight PL response at ambient pressure with a wavelength of about 662 nm. Although the intensity is low, PL can still be clearly observed and

the value is in good agreement with the previous reported (Ju et al., 2018). After further compression, PL shows remarkable red shift by about 727 nm at 12.6 GPa pressure as seen in figure 35a. More interestingly, a broad emission band is increasingly visible until it reaches the same maximum pressure. We know that at this pressure the phase begins to change from the alpha to the β -phase. Therefore, this drastic change in light emission is governed by the pressure-induced structural phase transformation as shown in the previous discussion. The effect of JT distortion plays an important role in changing the PL emission (Ma et al., 2018). Moreover, Figure 35b shows a further compression, PL emission sharply blue shift and decreases along and the intensity also decrease until finally disappears at 20.6 GPa. The PL evolution at β -phase transition coincides with the onset of an increase in the octahedral tilting.

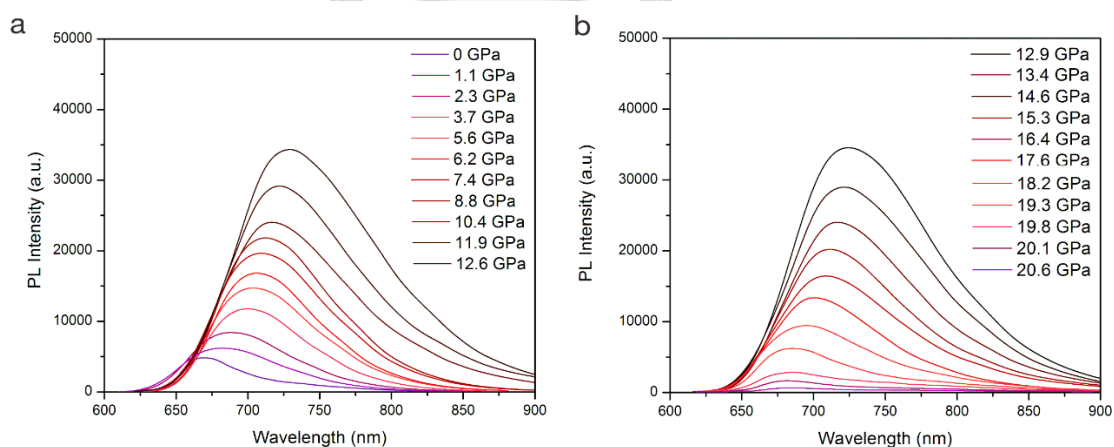


Figure 36. High-pressure photoluminescence properties of Cs_2TiBr_6 . Changes in the PL spectra of Cs_2TiBr_6 with pressure range 0-12.6 GPa (a) and 12.9-20.6 GPa (b).

The phase transitions are also evidenced by the piezochromism in double perovskite Cs_2TiBr_6 . As we can see in figure 36a, sample presents a similar transition to that observed in PL spectra upon comparison to 11.93 GPa, from transparent red to deep black. This indicates a drastically increasing wave length as shown in figure 36b. As previously discussed, this wavelength increases due to JT distortion in the α -phase transition. However, the color fades again from black to transparent red after the maximum pressure is achieved. It can be seen that the β -phase undergone a decrease in wavelength due to octahedral tilting. In addition, we also calculate the broad emission band with a full width at half maximum (FWHM) as a function of pressure as depicted in figure 36c. As we can see, the increase in wave length is accompanied by an increase in FWHM with a maximum of 118 nm at a pressure of 11.93 GPa. This indicates that the broad emission band occurs when the structure changes to P4/mnc due to the effect of JT distortion. When the pressure reaches 20.6 GPa, the FWHM of the PL peak rapidly drops. We credit the formation of STEs for this. One well-known mechanism for the substantial Stokes shifts seen in a number of broadly emitting lead halide perovskites, including the recently described two-dimensional (2D), one-dimensional (1D), and zero-dimensional (0D) system, is the radiative recombination of STEs (Lv et al., 2019; Ma et al., 2018).

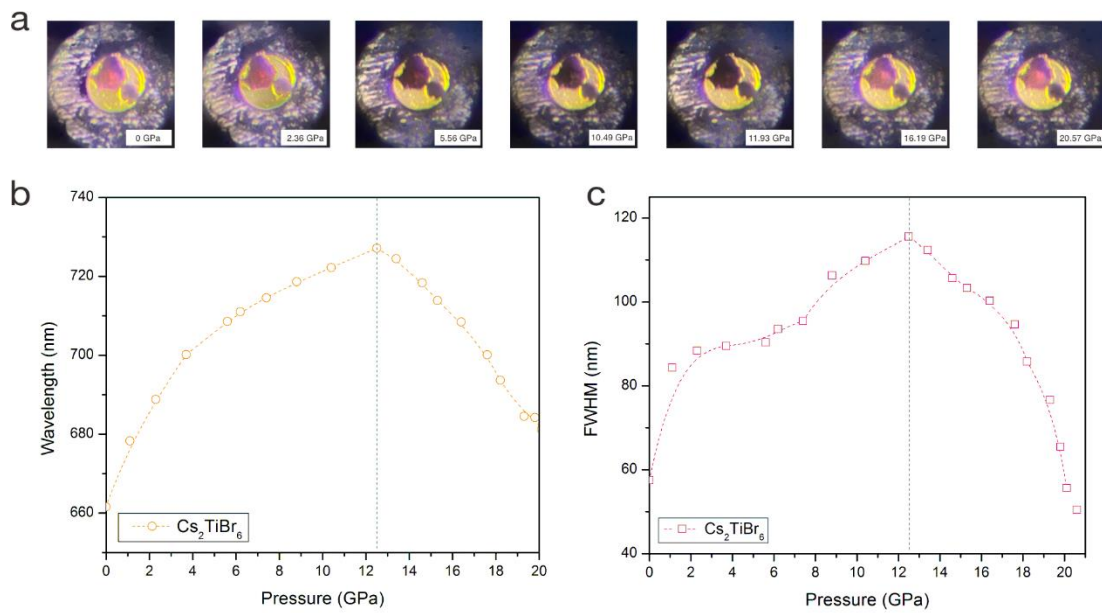


Figure 37. Optical micrographs of Cs_2TiBr_6 in a DAC, showing piezochromic transitions from translucent red to dark black (a). PL peak position (b) and full width at half-maximum (FWHM) (c) as a function of pressure during compression.

Previously, the optical transition's pressure-induced energy changes were connected to the direct energy gap. The experimental data was fitted using a linear pressure-dependent fit function, with the least-square method $E(P) = E(0) + \alpha P$. Since the quadratic equation was used to fit the pressure dependence of the band gap, so $E(P) = E(0) + \alpha P + \beta P^2$ where the pressure P is in GPa and the energy E is in eV. The pressure coefficient α is obtained by finding the data's best fit. A direct determination of the estimated hydrostatic deformation potential for the band gap is made possible by the application of hydrostatic pressure, which results in a shift of the conduction-band edge in relation to the valence-band edge due to a change in

volume. However, based on the concept of the deformation potential, $\alpha = \partial E / \partial \ln V$, it is possible to define the variation of the band gap with pressure in terms of the relative volume change by Murnaghan equation of state $\Delta E = \alpha(V - V_0)V$ (Murnaghan, 1944).

The schematic illustration of the emission process at ambient pressure in the double perovskite of Cs_2TlBr_6 is depicted in Figure 37a. The carrier is easily excited from the valance band to the conduction band and is localized to form a free exciton. Previous work describes this condition due to strong electron phonon coupling and strong quantum confinement (Zelewski et al., 2019). Free exciton is typically relax to a self-trapped exciton state as follows black arrow. STE radiation recombination occurs when the emission as indicated by dash line appears. The total emission energy can be described as follows:

$$E_{PL} = E_g - E_{st} - E_b - E_d \quad (2.13)$$

Where, E_{PL} , E_g , E_{st} , E_b , and E_d are photoluminescence energy, gap energy, self-trapped energy, binding energy, and deformation energy, respectively.

After the phase transforms from cubic to tetragonal at 11.93 GPa, JT distortion in octahedral gives more STE states as we can see in figure 37b. the extended STE states leads to broad-band-emission in distorted structure of Cs_2TlBr_6 indicated by a dash line. However, after pressure beyond 11.93, The sudden blue-shift in PL energy

at the phase transition can be attributed to the reduction in orbital overlap caused by octahedral tilting.

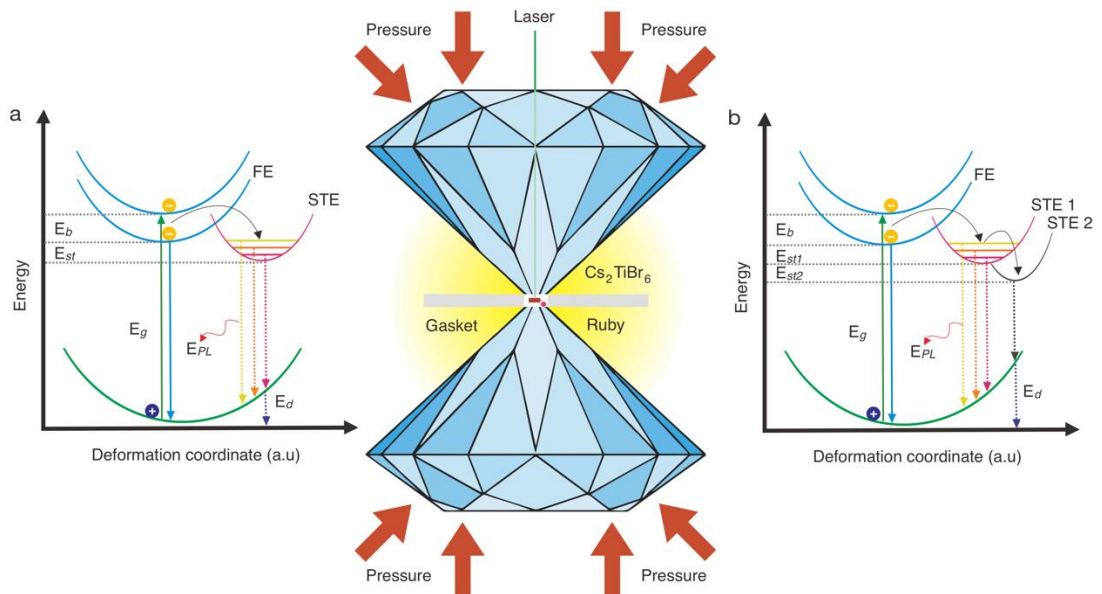


Figure 38. Pressure-induced emission mechanism associated with STE in Cs_2TiBr_6 .

Schematic configuration coordinate of emission for Cs_2TiBr_6 at ambient pressure (a)

and high-pressure (b).

CHULALONGKORN UNIVERSITY

CHAPTER 5

CONCLUSION

Perovskite materials are one of the promising candidates for energy applications such as data storage memory, light sensors, LEDs, optoelectronic devices, and others. The reverse temperature crystallization method was used to prepare single crystals of MAPbI₃. Crystal bulk from heating in the oil bath was found to be dark black in color with a diameter of ~1 mm. Raman spectroscopy was used to identify the vibrational properties of MAPbI₃. We have observed at least 8 vibration modes across 50 cm⁻¹ to 1500 cm⁻¹. The possible active mode of MAPbI₃ from low to high frequencies are the Pb-I stretching modes, MA torsion modes, MA translation modes, MA rocking modes, and hydrogen vibration modes. Overall, the observations that have been made are quite similar from the DFT calculation. We have reported on pressure-induced Raman modes by using DAC. Then, we found at least three phases under pressure of up to 5.34 GPa. At ambient pressure, the structural fluctuation due to freely motion of MA can be assumed as dynamic phase of MAPbI₃. In addition, the peaks of N-H bending modes indicate that the H movement does not interact with the PbI₃ framework. At 3.26 GPa, the new phase is static phase which is observed as saturated intensity of internal vibration MA due to the distorted PbI₃ framework.

We also propose a lead-free double perovskite-based perovskite material to avoid potential toxic devices. The double perovskite Ti-based HPs are more stable than Pb-based HPs in terms of reliability. We have prepared the double perovskite by using solution synthesis method. XRD was used to ensure the purity and determine the structure of Cs_2TiBr_6 and suggested as cubic phase $\text{Fm}\bar{3}\text{m}$ with lattice constant around 10.87 \AA . Then, we observed the vibrational properties by using Raman spectroscopy across frequency range 50 cm^{-1} to 750 cm^{-1} . We found five major peaks corresponding to two vibrational modes of CsBr and three vibrational modes of octahedral TiBr_6 in ambient pressure. the α -phase observes under ambient conditions. After the pressure reaches 8.8 GPa until 10.4 GPa, new peaks are appeared around 408.3 cm^{-1} and 613.7 cm^{-1} indicates the transition α -phase to β -phase. Above 11.9 GPa, the phase completely changes and gives strong octahedral interaction. the PL emission shows remarkable red shift and broadening upon compression up to 12.6 GPa which is indicate that the JT distortion plays an important role for giving more self-trap exciton (STE) states.

REFERENCES

- Alfè, D., Gillan, M., & Price, G. D. (2002). Composition and temperature of the Earth's core constrained by combining ab initio calculations and seismic data. *Earth and Planetary Science Letters*, 195(1-2), 91-98.
- Alsalloum, A. Y., Turedi, B., Zheng, X., Mitra, S., Zhumekenov, A. A., Lee, K. J., Maity, P., Gereige, I., AlSaggaf, A., & Roqan, I. S. (2020). Low-temperature crystallization enables 21.9% efficient single-crystal MAPbI₃ inverted perovskite solar cells. *ACS Energy Letters*, 5(2), 657-662.
- Baikie, T., Fang, Y., Kadro, J. M., Schreyer, M., Wei, F., Mhaisalkar, S. G., Graetzel, M., & White, T. J. (2013). Synthesis and crystal chemistry of the hybrid perovskite (CH₃NH₃)PbI₃ for solid-state sensitized solar cell applications. *Journal of Materials Chemistry A*, 1(18), 5628-5641.
- [Record #35 is using a reference type undefined in this output style.]
- bin Mohd Yusoff, A. R., Mahata, A., Vasilopoulou, M., Ullah, H., Hu, B., da Silva, W. J., Schneider, F. K., Gao, P., Ievlev, A. V., & Liu, Y. (2021). Observation of large Rashba spin-orbit coupling at room temperature in compositionally engineered perovskite single crystals and application in high performance photodetectors. *Materials today*, 46, 18-27.
- Brivio, F., Butler, K. T., Walsh, A., & Van Schilfegaarde, M. (2014). Relativistic quasiparticle self-consistent electronic structure of hybrid halide perovskite photovoltaic absorbers. *Physical Review B*, 89(15), 155204.
- Brivio, F., Walker, A. B., & Walsh, A. (2013). Structural and electronic properties of hybrid perovskites for high-efficiency thin-film photovoltaics from first-principles. *Applied Materials*, 1(4), 042111.
- Buriak, J. M., Kamat, P. V., Schanze, K. S., Alivisatos, A. P., Murphy, C. J., Schatz, G. C. (2017). Virtual Issue on Metal-Halide Perovskite Nanocrystals—A Bright Future for Optoelectronics. *Chemistry of Materials*, 29(21), 8915-8917. <https://doi.org/10.1021/acs.chemmater.7b04336>
- Cabana, A., & Sandorfy, C. (1962). The infrared spectra of solid methylammonium

- halides. *Spectrochimica Acta*, *18*(6), 843-861.
- Capitani, F., Marini, C., Caramazza, S., Postorino, P., Garbarino, G., Hanfland, M., Pisanu, A., Quadrelli, P., & Malavasi, L. (2016). High-pressure behavior of methylammonium lead iodide (MAPbI₃) hybrid perovskite. *Journal of applied physics*, *119*(18), 185901.
- Chen, M., Ju, M.-G., Carl, A. D., Zong, Y., Grimm, R. L., Gu, J., Zeng, X. C., Zhou, Y., & Padture, N. P. (2018). Cesium Titanium(IV) Bromide Thin Films Based Stable Lead-free Perovskite Solar Cells. *Joule*, *2*(3), 558-570. <https://doi.org/10.1016/j.joule.2018.01.009>
- Chen, Q., De Marco, N., Yang, Y., Song, T.-B., Chen, C.-C., Zhao, H., Hong, Z., Zhou, H., & Yang, Y. (2015). Under the spotlight: The organic-inorganic hybrid halide perovskite for optoelectronic applications. *Nano Today*, *10*(3), 355-396. <https://doi.org/https://doi.org/10.1016/j.nantod.2015.04.009>
- Cho, Y. J., Jeong, M. J., Park, J. H., Hu, W., Lim, J., & Chang, H. S. (2021). Charge Transporting Materials Grown by Atomic Layer Deposition in Perovskite Solar Cells. *Energies*, *14*(4), 1156.
- Dubrovinsky, L., Dubrovinskaia, N., Prakapenka, V. B., & Abakumov, A. M. (2012). Implementation of micro-ball nanodiamond anvils for high-pressure studies above 6 Mbar. *Nature communications*, *3*(1), 1-7.
- EIA, E. I. A. (2021). *International Energy Outlook 2021*. U.S. Department of Energy. <https://www.eia.gov/outlooks/ieo/>
- Eperon, G. E., Paternò, G. M., Sutton, R. J., Zampetti, A., Haghighirad, A. A., Cacialli, F., & Snaith, H. J. (2015). Inorganic caesium lead iodide perovskite solar cells. *Journal of Materials Chemistry A*, *3*(39), 19688-19695.
- Euvrard, J., Wang, X., Li, T., Yan, Y., & Mitzi, D. B. (2020). Is Cs₂TiBr₆ a promising Pb-free perovskite for solar energy applications? *Journal of Materials Chemistry A*, *8*(7), 4049-4054.
- Fu, R., Chen, Y., Yong, X., Ma, Z., Wang, L., Lv, P., Lu, S., Xiao, G., & Zou, B. (2019). Pressure-induced structural transition and band gap evolution of double perovskite Cs₂AgBiBr₆ nanocrystals. *Nanoscale*, *11*(36), 17004-17009.
- Giustino, F., & Snaith, H. J. (2016). Toward lead-free perovskite solar cells. *ACS Energy*

Letters, 1(6), 1233-1240.

[Record #63 is using a reference type undefined in this output style.]

He, Y., Guo, X., Zheng, H., Xv, L., & Li, S. (2022). Stability investigation of the titanium-based eco-friendly perovskite-like antiferroite Cs₂TiBr₆. *Journal of Materials Chemistry C*, 10(24), 9301-9309.

Jaffe, A., Lin, Y., Beavers, C. M., Voss, J., Mao, W. L., & Karunadasa, H. I. (2016). High-pressure single-crystal structures of 3D lead-halide hybrid perovskites and pressure effects on their electronic and optical properties. *ACS central science*, 2(4), 201-209.

Jaffe, A., Lin, Y., & Karunadasa, H. I. (2017). Halide Perovskites under Pressure: Accessing New Properties through Lattice Compression. *ACS Energy Letters*, 2(7), 1549-1555. <https://doi.org/10.1021/acsenerylett.7b00284>

Jaffe, A., Lin, Y., Mao, W. L., & Karunadasa, H. I. (2017). Pressure-induced metallization of the halide perovskite (CH₃NH₃)PbI₃. *Journal of the American Chemical Society*, 139(12), 4330-4333.

Jiang, J., Niu, G., Sui, L., Wang, X., Zhang, Y., Che, L., Wu, G., Yuan, K., & Yang, X. (2021). Transformation between the Dark and Bright Self-Trapped Excitons in Lead-Free Double-Perovskite Cs₂NaBiCl₆ under Pressure. *The Journal of Physical Chemistry Letters*, 12(30), 7285-7292.

Jiang, S., Fang, Y., Li, R., Xiao, H., Crowley, J., Wang, C., White, T. J., Goddard III, W. A., Wang, Z., & Baikie, T. (2016). Pressure-Dependent Polymorphism and Band-Gap Tuning of Methylammonium Lead Iodide Perovskite. *Angewandte Chemie*, 128(22), 6650-6654.

Ju, M.-G., Chen, M., Zhou, Y., Garces, H. F., Dai, J., Ma, L., Padture, N. P., & Zeng, X. C. (2018). Earth-Abundant Nontoxic Titanium(IV)-based Vacancy-Ordered Double Perovskite Halides with Tunable 1.0 to 1.8 eV Bandgaps for Photovoltaic Applications. *ACS Energy Letters*, 3(2), 297-304. <https://doi.org/10.1021/acsenerylett.7b01167>

Kamisuki, T., & Maeda, S. (1973). The resonance raman effect of TiBr₄ and TiI₄. *Chemical Physics Letters*, 19(3), 379-382.

- Kong, L., Liu, G., Gong, J., Hu, Q., Schaller, R. D., Dera, P., Zhang, D., Liu, Z., Yang, W., Zhu, K., Tang, Y., Wang, C., Wei, S.-H., Xu, T., & Mao, H.-k. (2016). Simultaneous band-gap narrowing and carrier-lifetime prolongation of organic–inorganic trihalide perovskites. *Proceedings of the National Academy of Sciences*, *113*(32), 8910. <https://doi.org/10.1073/pnas.1609030113>
- Li, N., Manoun, B., Tang, L., Ke, F., Liu, F., Dong, H., Lazor, P., & Yang, W. (2016). Pressure-Induced Structural and Electronic Transition in Sr₂ZnWO₆ Double Perovskite. *Inorganic Chemistry*, *55*(13), 6770-6775. <https://doi.org/10.1021/acs.inorgchem.6b01091>
- Li, Q., Wang, Y., Pan, W., Yang, W., Zou, B., Tang, J., & Quan, Z. (2017). High-Pressure Band-Gap Engineering in Lead-Free Cs₂AgBiBr₆ Double Perovskite. *Angewandte Chemie International Edition*, *56*(50), 15969-15973. <https://doi.org/https://doi.org/10.1002/anie.201708684>
- Li, Z., Yang, M., Park, J.-S., Wei, S.-H., Berry, J. J., & Zhu, K. (2016). Stabilizing Perovskite Structures by Tuning Tolerance Factor: Formation of Formamidinium and Cesium Lead Iodide Solid-State Alloys. *Chemistry of Materials*, *28*(1), 284-292. <https://doi.org/10.1021/acs.chemmater.5b04107>
- Liang, J., Zhao, P., Wang, C., Wang, Y., Hu, Y., Zhu, G., Ma, L., Liu, J., & Jin, Z. (2017). CsPb_{0.9}Sn_{0.1}Br₂ based all-inorganic perovskite solar cells with exceptional efficiency and stability. *Journal of the American Chemical Society*, *139*(40), 14009-14012.
- Liu, D., Zeng, H., Huang, Y., Zheng, G., & Sa, R. (2021). Pressure-induced band gap tuning in Cs₂TiBr₆: A theoretical study. *Journal of Solid State Chemistry*, *300*, 122244. <https://doi.org/https://doi.org/10.1016/j.jssc.2021.122244>
- Lü, X., Yang, W., Jia, Q., & Xu, H. (2017). Pressure-induced dramatic changes in organic–inorganic halide perovskites. *Chemical science*, *8*(10), 6764-6776.
- Lv, C., Yang, X., Shi, Z., Wang, L., Sui, L., Li, Q., Qin, J., Liu, K., Zhang, Z., & Li, X. (2019). Pressure-induced ultra-broad-band emission of a Cs₂AgBiBr₆ perovskite thin film. *The Journal of Physical Chemistry C*, *124*(2), 1732-1738.
- Ma, Z., Liu, Z., Lu, S., Wang, L., Feng, X., Yang, D., Wang, K., Xiao, G., Zhang, L., & Redfern, S. A. (2018). Pressure-induced emission of cesium lead halide

- perovskite nanocrystals. *Nature communications*, *9*(1), 1-8.
- Matsuishi, K., Ishihara, T., Onari, S., Chang, Y., & Park, C. (2004). Optical properties and structural phase transitions of lead-halide based inorganic–organic 3D and 2D perovskite semiconductors under high pressure. *physica status solidi (b)*, *241*(14), 3328-3333.
- Monroy, G. L., Fitzgerald, S. T., Locke, A., Won, J., Spillman, J., Darold R, Ho, A., Zaki, F. R., Choi, H., Chaney, E. J., & Werkhaven, J. A. (2022). Multimodal handheld probe for characterizing otitis media—integrating Raman spectroscopy and optical coherence tomography. *Frontiers in Photonics*, *3*, 929574.
- Mosca, S., Conti, C., Stone, N., & Matousek, P. (2021). Spatially offset Raman spectroscopy. *Nature Reviews Methods Primers*, *1*(1), 1-16.
- Murnaghan, F. D. (1944). The compressibility of media under extreme pressures. *Proceedings of the National Academy of Sciences*, *30*(9), 244-247.
- Nguyen, L. A. T., Minh, D. N., Zhang, D., Wang, L., Kim, J., & Kang, Y. (2020). Pressure-Induced Selective Amorphization of CsPbBr₃ for the Purification of Cs₄PbBr₆. *The Journal of Physical Chemistry C*, *124*(40), 22291-22297.
- O'Bannon III, E. F., Jenei, Z., Cynn, H., Lipp, M. J., & Jeffries, J. R. (2018). Contributed Review: Culet diameter and the achievable pressure of a diamond anvil cell: Implications for the upper pressure limit of a diamond anvil cell. *Review of Scientific Instruments*, *89*(11), 111501.
- Onoda-Yamamuro, N., Matsuo, T., & Suga, H. (1990). Calorimetric and IR spectroscopic studies of phase transitions in methylammonium trihalogenoplumbates (II). *Journal of Physics and Chemistry of Solids*, *51*(12), 1383-1395.
- Ou, T., Yan, J., Xiao, C., Shen, W., Liu, C., Liu, X., Han, Y., Ma, Y., & Gao, C. (2016). Visible light response, electrical transport, and amorphization in compressed organolead iodine perovskites. *Nanoscale*, *8*(22), 11426-11431.
- Pang, S., Hu, H., Zhang, J., Lv, S., Yu, Y., Wei, F., Qin, T., Xu, H., Liu, Z., & Cui, G. (2014). NH₂CH₃NH₂PbI₃: an alternative organolead iodide perovskite sensitizer for mesoscopic solar cells. *Chemistry of Materials*, *26*(3), 1485-1491.
- Park, M., Kornienko, N., Reyes-Lillo, S. E., Lai, M., Neaton, J. B., Yang, P., & Mathies, R. A.

- (2017). Critical role of methylammonium librational motion in methylammonium lead iodide (CH₃NH₃PbI₃) perovskite photochemistry. *Nano letters*, 17(7), 4151-4157.
- Park, N.-G. (2015). Perovskite solar cells: an emerging photovoltaic technology. *Materials today*, 18(2), 65-72.
- Pei, C., & Wang, L. (2019). Recent progress on high-pressure and high-temperature studies of fullerenes and related materials. *Matter and Radiation at Extremes*, 4(2), 028201. <https://doi.org/10.1063/1.5086310>
- Perez-Osorio, M. A., Champagne, A., Zacharias, M., Rignanese, G.-M., & Giustino, F. (2017). Van der Waals interactions and anharmonicity in the lattice vibrations, dielectric constants, effective charges, and infrared spectra of the organic–inorganic halide perovskite CH₃NH₃PbI₃. *The Journal of Physical Chemistry C*, 121(34), 18459-18471.
- Perez-Osorio, M. A., Lin, Q., Phillips, R. T., Milot, R. L., Herz, L. M., Johnston, M. B., & Giustino, F. (2018). Raman spectrum of the organic–inorganic halide perovskite CH₃NH₃PbI₃ from first principles and high-resolution low-temperature Raman measurements. *The Journal of Physical Chemistry C*, 122(38), 21703-21717.
- Pérez-Osorio, M. A., Milot, R. L., Filip, M. R., Patel, J. B., Herz, L. M., Johnston, M. B., & Giustino, F. (2015). Vibrational properties of the organic–inorganic halide perovskite CH₃NH₃PbI₃ from theory and experiment: factor group analysis, first-principles calculations, and low-temperature infrared spectra. *The Journal of Physical Chemistry C*, 119(46), 25703-25718.
- Raman, C. V., & Krishnan, K. S. (1928). A new type of secondary radiation. *Nature*, 121(3048), 501-502.
- Ruoff, A. L., Xia, H., Luo, H., & Vohra, Y. K. (1990). Miniaturization techniques for obtaining static pressures comparable to the pressure at the center of the earth: X-ray diffraction at 416 GPa. *Review of Scientific Instruments*, 61(12), 3830-3833.
- Saidaminov, M. I., Abdelhady, A. L., Murali, B., Alarousu, E., Burlakov, V. M., Peng, W., Dursun, I., Wang, L., He, Y., & Maculan, G. (2015). High-quality bulk hybrid perovskite single crystals within minutes by inverse temperature crystallization.

Nature communications, 6(1), 1-6.

- Shen, P., Vogt, T., & Lee, Y. (2020). Pressure-Induced Enhancement of Broad-Band White Light Emission in Butylammonium Lead Bromide. *The Journal of Physical Chemistry Letters*, 11(10), 4131-4137. <https://doi.org/10.1021/acs.jpcllett.0c01160>
- Shockley, W., & Queisser, H. J. (1961). Detailed balance limit of efficiency of p-n junction solar cells. *Journal of applied physics*, 32(3), 510-519.
- Slavney, A. H., Hu, T., Lindenberg, A. M., & Karunadasa, H. I. (2016). A bismuth-halide double perovskite with long carrier recombination lifetime for photovoltaic applications. *Journal of the American Chemical Society*, 138(7), 2138-2141.
- Stranks, S. D., Eperon, G. E., Grancini, G., Menelaou, C., Alcocer, M. J., Leijtens, T., Herz, L. M., Petrozza, A., & Snaith, H. J. (2013). Electron-hole diffusion lengths exceeding 1 micrometer in an organometal trihalide perovskite absorber. *Science*, 342(6156), 341-344.
- Swainson, I., Tucker, M., Wilson, D., Winkler, B., & Milman, V. (2007). Pressure response of an organic– inorganic perovskite: methylammonium lead bromide. *Chemistry of Materials*, 19(10), 2401-2405.
- Szafranski, M., & Katrusiak, A. (2016). Mechanism of pressure-induced phase transitions, amorphization, and absorption-edge shift in photovoltaic methylammonium lead iodide. *The Journal of Physical Chemistry Letters*, 7(17), 3458-3466.
- Tao, S., Schmidt, I., Brocks, G., Jiang, J., Tranca, I., Meerholz, K., & Olthof, S. (2019). Absolute energy level positions in tin- and lead-based halide perovskites. *Nature communications*, 10(1), 2560. <https://doi.org/10.1038/s41467-019-10468-7>
- Umari, P., Mosconi, E., & De Angelis, F. (2014). Relativistic GW calculations on CH₃NH₃PbI₃ and CH₃NH₃SnI₃ perovskites for solar cell applications. *Scientific reports*, 4(1), 1-7.
- Wang, Y., Lü, X., Yang, W., Wen, T., Yang, L., Ren, X., Wang, L., Lin, Z., & Zhao, Y. (2015). Pressure-induced phase transformation, reversible amorphization, and anomalous visible light response in organolead bromide perovskite. *Journal of the American Chemical Society*, 137(34), 11144-11149.

- WEC, W. E. C. (2013). *World Energy Resources: Solar*. https://www.worldenergy.org/assets/images/imported/2013/10/WER_2013_8_Solar_revised.pdf
- Xie, L.-Q., Zhang, T.-Y., Chen, L., Guo, N., Wang, Y., Liu, G.-K., Wang, J.-R., Zhou, J.-Z., Yan, J.-W., & Zhao, Y.-X. (2016). Organic–inorganic interactions of single crystalline organolead halide perovskites studied by Raman spectroscopy. *Physical Chemistry Chemical Physics*, *18*(27), 18112-18118.
- Yin, T., Fang, Y., Chong, W. K., Ming, K. T., Jiang, S., Li, X., Kuo, J. L., Fang, J., Sum, T. C., & White, T. J. (2018). High-Pressure-Induced Comminution and Recrystallization of CH₃NH₃PbBr₃ Nanocrystals as Large Thin Nanoplates. *Advanced Materials*, *30*(2), 1705017.
- Yoshimura, M., & Sardar, K. (2021). Revisiting the valence stability and preparation of perovskite structure type oxides ABO₃ with the use of Madelung electrostatic potential energy and lattice site potential. *RSC Advances*, *11*(34), 20737-20745.
- Zelewski, S., Urban, J., Surrente, A., Maude, D. K., Kuc, A., Schade, L., Johnson, R., Dollmann, M., Nayak, P., & Snaith, H. (2019). Revealing the nature of photoluminescence emission in the metal-halide double perovskite Cs₂AgBiBr₆. *Journal of Materials Chemistry C*, *7*(27), 8350-8356.
- Zhang, L., Wang, Y., Lv, J., & Ma, Y. (2017). Materials discovery at high pressures. *Nature Reviews Materials*, *2*(4), 17005. <https://doi.org/10.1038/natrevmats.2017.5>
- Zhang, L., Zeng, Q., & Wang, K. (2017). Pressure-induced structural and optical properties of inorganic halide perovskite CsPbBr₃. *The Journal of Physical Chemistry Letters*, *8*(16), 3752-3758.
- Zhang, Y., Liu, Y., Yang, Z., & Liu, S. F. (2018). High-quality perovskite MAPbI₃ single crystals for broad-spectrum and rapid response integrate photodetector. *Journal of energy chemistry*, *27*(3), 722-727.
- Zhao, X.-G., Yang, J.-H., Fu, Y., Yang, D., Xu, Q., Yu, L., Wei, S.-H., & Zhang, L. (2017). Design of lead-free inorganic halide perovskites for solar cells via cation-transmutation. *Journal of the American Chemical Society*, *139*(7), 2630-2638.
- Zhou, H., Chen, Q., Li, G., Luo, S., Song, T.-b., Duan, H.-S., Hong, Z., You, J., Liu, Y., &

Yang, Y. (2014). Interface engineering of highly efficient perovskite solar cells. *Science*, 345(6196), 542-546. <https://doi.org/10.1126/science.1254050>





จุฬาลงกรณ์มหาวิทยาลัย
CHULALONGKORN UNIVERSITY

VITA

NAME	Ardimas
DATE OF BIRTH	28 November 1992
PLACE OF BIRTH	Magelang
INSTITUTIONS ATTENDED	Universitas Islam Negeri Sunan Kalijaga, Yogyakarta, Indonesia Prince of Songkla University, Hatyai, Thailand
HOME ADDRESS	Dogaten 04/01 Sukorejo, Sub. Dis. Mertoyudan, Dis. Magelang, Prov. Jawa Tengah
PUBLICATION	Ardimas, Putson, C., 2017. Enhanced Dielectric and Electrical Properties in Polyurethane Composites with Graphene Nanosheets. Materials Science Forum. Ardimas, Putson, C., 2018. High Electromechanical Performance of Modified Polyurethane Three-Phase Composites. Composites Science and Technology.
AWARD RECEIVED	2017 6th International Conference on Material Science and Engineering Technology as Best Oral Presentation, Seoul National University (SNU), Seoul, Republic of Korea